Convectively Coupled Equatorial Wave Simulations Using the ECMWF IFS and the NOAA GFS Cumulus Convection Schemes in the NOAA GFS Model

LISA BENGTSSON,[a,b] JULIANA DIAS,[a,b] MARIA GEHNE,[a,b] PETER BECHTOLD,[c] JEFFREY WHITAKER,[b] JIAN-WEN BAO,[b] LINUS MAGNUSSON,[c] SARA MICHELSON,[a,b] PHILIP PEGION,[a,b] STEFAN TULICH,[a,b] AND GEORGE N. KILADIS[b]

[a] *CIRES, University of Colorado Boulder, Boulder, Colorado*
[b] *NOAA/Earth System Research Laboratory, Boulder, Colorado*
[c] *European Centre for Medium-Range Weather Forecasts, Reading, United Kingdom*

(Manuscript received 12 June 2019, in final form 16 August 2019)

ABSTRACT

There is a longstanding challenge in numerical weather and climate prediction to accurately model tropical wave variability, including convectively coupled equatorial waves (CCEWs) and the Madden–Julian oscillation. For subseasonal prediction, the European Centre for Medium-Range Weather Forecasts (ECMWF) Integrated Forecasting System (IFS) has been shown to be superior to the NOAA Global Forecast System (GFS) in simulating tropical variability, suggesting that the ECMWF model is better at simulating the interaction between cumulus convection and the large-scale tropical circulation. In this study, we experiment with the cumulus convection scheme of the ECMWF IFS in a research version of the GFS to understand which aspects of the IFS cumulus convection scheme outperform those of the GFS convection scheme in the tropics. We show that the IFS cumulus convection scheme produces significantly different tropical moisture and temperature tendency profiles from those simulated by the GFS convection scheme when it is coupled with other physics schemes in the GFS physics package. We show that a consistent treatment of the interaction between parameterized convective plumes in the GFS planetary boundary layer (PBL) and the IFS convection scheme is required for the GFS to replicate the tropical temperature and moisture profiles simulated by the IFS model. The GFS model with the IFS convection scheme, and the consistent treatment between the convection and PBL schemes, produces much more organized convection in the tropics, and generates tropical waves that propagate more coherently than the GFS in its default configuration due to better simulated interaction between low-level convergence and precipitation.

1. Introduction

Convectively coupled equatorial waves (CCEWs) are fundamental modes of tropical variability (Kiladis et al. 2009; Zhang 2005), spanning a few days (e.g., inertia–gravity and Kelvin waves) to several weeks [equatorial Rossby (ER) waves and the Madden–Julian oscillation (MJO)]. These disturbances are of practical importance because they modulate tropical weather and affect remote weather through tropical to extratropical teleconnections (e.g., Schreck et al. 2013; Jones et al. 2011). Because the initiation and propagation of these disturbances inherently depends on processes that are only partially resolved in global prediction systems, CCEWs have been a major modeling challenge from weather to climate scales.

The problem of modeling CCEWs is further complicated by the fact that the behavior of the moisture convection–circulation coupling is apparently different for different types of disturbances. For instance, in some cases, analogous ''dry'' modes exist without convective coupling [e.g., Matsuno (1966) modes], and others like the MJO are thought to be ''moisture modes'' (Sobel and Maloney 2013) with no dry counterpart. While the role of moisture coupling might vary, studies have indicated that moistening by shallow and congestus convection is critical for CCEW initiation and propagation (e.g., Mapes et al. 2006). A common problem among models with parameterized convection is that the transition from shallow to deep convection generally occurs too fast, leading to insufficient heating and divergent circulation at low levels (Frierson 2007; Lin et al. 2008; Thayer-Calder and Randall 2009; Hirons et al. 2013a). Therefore, parameterizations of subgrid processes related

Corresponding author: Lisa Bengtsson, lisa.bengtsson@noaa.gov

DOI: 10.1175/MWR-D-19-0195.1

to clouds and precipitation, and their feedback with dynamics, are thought to be a primary source of errors in CCEW prediction.

In recent years, novel methods of parameterizing cumulus convection have proven successful at improving tropical variability (e.g., Bechtold et al. 2008; Chikira and Sugiyama 2013; Park 2014; Goswami et al. 2017). It is argued in these studies that stronger entrainment and/or convective rain evaporation helps increase the cumulus parameterization sensitivity to tropospheric moisture, yielding more realistic transitions from shallow to deep convection, and, therefore, to better representation of CCEWs. However, this improvement in tropical variability is model-specific and may also come along with a degraded mean climate (Kim et al. 2011). With a focus on subseasonal predictions, the ECMWF system stands out in performance in the tropics (Janiga et al. 2018; Dias et al. 2018; Lim et al. 2018), which has been largely attributed to revisions in their convective parameterization (e.g., Vitart 2014; Hirons et al. 2013a,b).

The National Oceanic and Atmospheric Association's (NOAA) current (spring 2019) prediction models generally do not capture the evolution of CCEWs with much fidelity. For example, a recent version of NOAA's Global Ensemble Forecast System (GEFS) moved the MJO too slowly and decreased its amplitude too rapidly (Hamill and Kiladis 2014). Similarly, Goswami et al. (2017) showed that NOAA's Climate Forecast System version 2 (CFSv2) in climate simulations underestimates the power of all CCEW modes. In a recent study, motivated by the El Niño Rapid Response (ENRR) field campaign (Dole et al. 2018), Dias et al. (2018) studied two global NWP systems in their ability to simulate equatorial waves. The models analyzed were the NOAA GFS v14 and the ECMWF Integrated Forecasting System (IFS). One of their conclusions was that while both systems produce very good short-range forecasts of rainfall with similar mean patterns, the IFS model better represents coherence between low-level divergence and rainfall associated with the MJO, and the Matsuno (1966) modes [see Fig. 11 in Dias et al. (2018)], implying that the IFS model is superior in maintaining such disturbances. Since the initial state and short-range forecasts do a good job at capturing rainfall in both systems, it is hypothesized in their study that the degraded forecast with lead time in the GFS could be attributed to the cumulus parameterization, or its interaction with other physical parameterizations, rather than the initialization.

In the present study, we implement the cumulus convection scheme (representing deep, shallow, and midlevel convection) from the ECMWF IFS cycle 45r1 model into a research version of the GFS. In addition, we run the GFS with both initial conditions from the GFS analysis and the ECMWF IFS analysis. The aim is to study the impact that the IFS cumulus convection scheme has on CCEW modes in the GFS. We also investigate the relative role played by the initial conditions and the model physics for predicting such wave modes in the forecast. We investigate the behavior of the scheme in short-lead-time forecasts (out to 5 days), as well as seasonal forecasts (out to 90 days) to understand if the cumulus convection schemes influence CCEWs well beyond their initializations. Since physical parameterizations interact in a complex manner, some adjustments had to be made within the GFS physical parameterizations upon implementation of the IFS convection scheme to avoid erroneous feedbacks and introduction of model biases, as we next describe. In a related study, Bassill (2015) discussed in the Weather Research and Forecasting (WRF) Model framework improved forecast skill with an adapted version of the IFS scheme with respect to SAS (as implemented in WRF), that mainly stems from the stronger convective entrainment and increased sensitivity to moisture.

2. Methodology

The version of the GFS used in this study is referred to as GFSv15.0.0. This model is the first version of the GFS using an updated dynamical core referred to as the finite volume cubed sphere (FV3; see, e.g., Lin and Rood 1996; Lin 2004; Putman and Lin 2007; Harris et al. 2016 and references therein), and a new cloud microphysics scheme referred to as the GFDL microphysics (Lin et al. 1983; Chen and Lin 2011, 2013). The GFDL cloud microphysics scheme is a one-moment bulk microphysics scheme using six prognostic water species. The planetary boundary layer (PBL) scheme is a first-order turbulent transport scheme (Han and Pan 2011; Han et al. 2017). It utilizes a ''hybrid'' eddy diffusion mass flux (EDMF) approach where the mixing by eddy diffusion is modeled by a so-called eddy-diffusivity countergradient mixing (Troen and Mahrt 1986; Hong and Pan 1996), and the mixing by convective plumes is modeled using a mass flux approach, following Siebesma et al. (2007). The shallow and deep cumulus parameterizations will be described in more detail below and are originally based on Arakawa and Schubert (1974), but has over the years seen substantial updates following Pan and Wu (1995), Han and Pan (2011), and Han et al. (2017). We refer to this cumulus scheme as scale-aware simplified Arakawa–Schubert (SASAS).

a. Description of the cumulus convection schemes

We implement the cumulus convection scheme present in cycle 45r1 of the ECMWF Integrated Forecasting

System (IFS), and replace the current operational SASAS shallow and deep cumulus parameterization schemes (Han and Pan 2011) in the GFS. The IFS convection scheme was originally described in Tiedtke et al. (1988), with many improvements implemented throughout the years as described in Gregory et al. (2000), Bechtold et al. (2008, 2014), and in the IFS cycle 45r1 documentation (2016). Below we summarize the main building blocks and differences in the two convection schemes.

1) CLOUD MODEL

A single-plume mass-flux scheme is used in both the SASAS and IFS-convection schemes to represent the bulk effects of individual clouds. The equations of balance for mass, heat, water vapor, hydrometeors, and momentum between the cloud and its environment are defined as functions of the mass entrainment minus the mass detrainment following the seminal work of Yanai et al. (1973). The formulation used for the entrainment in the IFS convection scheme is a function of relative humidity in order to increase the mass flux in unstable regions. This formulation for the entrainment in the updraft, using relative humidity, has been adapted by the SASAS scheme (with some minor modifications), and is described in Bechtold et al. (2008). In the IFS convection scheme, the detrainment formulation in the updraft is split into a ''turbulent'' and an ''organized'' part, where the turbulent part is, similarly to the entrainment, a function of relative humidity. The organized part of the detrainment is set proportional to the decrease in updraft vertical velocity with height. This is different from the SASAS scheme where the detrainment formulation only has the ''turbulent'' part which is a function of relative humidity (Bechtold et al. 2008; Han and Pan 2011). Also, importantly, the detrained cloud water profiles differ as the SASAS scheme only detrains cloud condensate from the layers above the level of the minimum moist static energy, whereas the IFS convection scheme allows for detrainment of cloud condensate into the gridscale cloud condensate throughout the whole cloud layer. We discuss the implications of this difference in the implementation below.

2) CLOSURE

In the SASAS scheme the closure assumes an equilibrium between large-scale forcing and subgrid-scale convection by relaxing the so-called cloud work function A toward a reference value A_0 over the adjustment time scale τ, following the pioneering work on quasi equilibrium of Arakawa and Schubert (1974). As the grid size becomes smaller, the quasi-equilibrium closure assumption is no longer valid, as there is an underlying assumption that the updraft area fraction of convection is much smaller than the environment fraction in a grid box, so that the convection is in statistical equilibrium with the large-scale flow, at steady state. Thus, for grid sizes smaller than a threshold value (currently set to be 8 km), the closure has been adapted by Han et al. (2017) to compute the cloud base mass flux in the deep convection scheme as a function of the mean updraft vertical velocity rather than using the Arakawa–Schubert quasi-equilibrium closure.

In the IFS, the closure for deep convection assumes an equilibrium between the forcing from the large-scale circulation, the surface and the convective stabilization. Thus, there is a relaxation time scale over which CAPE is reduced, that is dependent on model resolution and the amount of CAPE. The SASAS scheme has adapted this adjustment time scale from the IFS convection scheme, which is a function of the depth of the cloud and the updraft vertical velocity, as described in Bechtold et al. (2008).

3) TRIGGERING

In both the IFS scheme and the SASAS scheme, the activation of convection (and determination of active or suppressed mode of convection) is done in a very simplified ''first guess'' updraft computation that determines the cloud base level, that is, the lifting condensation level (LCL) in the IFS convection scheme, and the level of free convection (LFC) in the SASAS scheme. These cloud base levels are found by giving a parcel a ''push'' from a given starting level. In the IFS convection scheme, the parcel is lifted from the surface for shallow, and first model level for deep convection. In the SASAS scheme a convection starting level (CSL), defined as the level of maximum moist static energy between the surface and 700 hPa for deep convection, and within the PBL for shallow convection, is first found. Furthermore, some decision of convective cloud type in terms of the plume depth is made. The IFS convection scheme considers shallow, midlevel, and deep convection, whereas the SASAS scheme considers only shallow and deep convection.

b. Observational datasets and reanalysis

The study period for our analysis is January–March 2016. Two precipitation datasets are used to evaluate the model forecasts. The bias-corrected Climate Prediction Center morphing method (CMORPH; Joyce et al. 2004; Joyce and Janowiak 2005; NOAA 2015) and the Tropical Rainfall Measuring Mission 3B42v7 (TRMM; Huffman et al. 2007, 2012) precipitation estimates are both available at 3 hourly temporal and 0.25° horizontal resolution. Differences between 6 hourly

precipitation forecasts and observations are evaluated based on the mean absolute error (MAE), mean bias and pattern correlation from 15°S to 15°N. Confidence intervals are determined using 1000 random resampling realizations with replacement and then calculating the 5th and 95th percentiles of the estimated quantities (MAE, bias, etc.).

To evaluate model performance of some of the dynamical variables the ECMWF interim reanalysis (ERA-Interim, hereinafter ERAI; ECMWF 2009; Dee et al. 2011a) data were used. It should be noted, however, that while strongly constrained by observations, ERAI is not a completely independent verification since a 2006 version of the IFS convection scheme has been used therein. However, the current IFS convection scheme, as used in this study, is much more advanced.

c. *Implementation details*

A few preparatory steps are necessary to call the IFS cumulus scheme within the GFS. These include extraction of tendencies from the dynamics, radiation and PBL scheme to serve as input to the convection scheme, conversion of moist variables from mixing ratio to specific humidity, conversion of units and the sign of surface fluxes, and flipping the index of the model levels since the IFS scheme has the highest index at the first model level above the surface. Not surprisingly, there are complex interactions among the convection scheme, the radiation scheme, the PBL scheme, and the large-scale condensation scheme that are not trivial to detangle upon implementation. The way we have enhanced our understanding of the different physical process interactions is to utilize both a Single Column Model (SCM) version of the GFS (https://dtcenter.org/GMTB/gmtb_scm_doc/index.html), and full 3D runs to study output tendencies, mass-flux profiles, humidity and temperature profiles, radiation fluxes, precipitation, and cloud cover, and then to introduce appropriate modifications to try to reproduce the convection tendencies from the ECMWF IFS model cycle 45r1.

We first illustrate how the model performs if we implement the IFS convection schemes "as is," without addressing any interaction with other physics schemes, and without any tuning. For this, we use 5-day forecasts with daily initialization from 1 January to 31 March 2016. Figure 1 shows the global mean precipitation (mm h^{-1}), regridded from 25 km grid spacing to a 2.5° grid, over the period 1 January to 31 March 2016 for CMORPH precipitation estimates (Fig. 1a), the control run with the SASAS cumulus convection scheme (Fig. 1b), GFS with the IFS cumulus convection scheme implemented without any tuning or adjustments(Fig. 1c), and GFS with the IFS cumulus convection scheme implemented with some adjustments/tuning that address interaction with other physical parameterizations (discussed below; Fig. 1d). For all the model simulations the 96-h (4 day) forecast lead time is shown. In general, the mean patterns are similar in all the panels; however, it is clear that the version with the "untuned" IFS convection scheme severely overestimates precipitation over the oceans and underestimates precipitation over land. This overestimation of precipitation in the untuned version increases with lead time as seen in Figs. 1e and 1f, which show the precipitation bias and mean error, respectively. After careful consideration of model physics interactions upon implementation, and further tuning of key parameters in the IFS convection scheme, we reached a model version of the GFS using the IFS convection scheme that produces a similar global mean bias as the SASAS scheme (Fig. 1d). We next describe the steps made to reach this version.

1) Interaction with PBL scheme

To ensure that the tendencies output from the GFS cumulus convection schemes resemble those from the IFS model, we first analyze the time-averaged tendencies from the convection, large-scale condensation (cloud microphysics), radiation and PBL schemes in an idealized single column forecast (described in Firl 2017) of the Atmospheric Radiation Measurement (ARM) project Tropical Warm Pool–International Cloud Experiment (TWP-ICE) case. Here we compare the tendencies from the GFS Single Column Model, with the two convection schemes implemented, to the tendencies from the ECMWF IFS Single Column Model from the same case. This allows us to compare the tendency profiles of not only convection, but also how other physics parameterization schemes respond differently in the two respective model systems for this idealized case.

TWP-ICE was an airborne measurement campaign conducted in the region near Darwin, Australia, in early 2006. The data from the campaign have been used in many process-oriented studies, within the atmospheric science community (e.g., Davies et al. 2013; Petch et al. 2014). The time period of observations for the TWP-ICE case covered both suppressed and active monsoon events.

Figure 2 shows the time-averaged model humidity tendencies for the TWP-ICE case, which includes both the "suppressed" and the "active" periods mentioned above. The different colors represent the different physics parameterizations as indicated by the legend. The left panel (Fig. 2a) shows the output from the ECMWF IFS model version 45r1. The blue curve represents the time averaged humidity tendency from the convection schemes

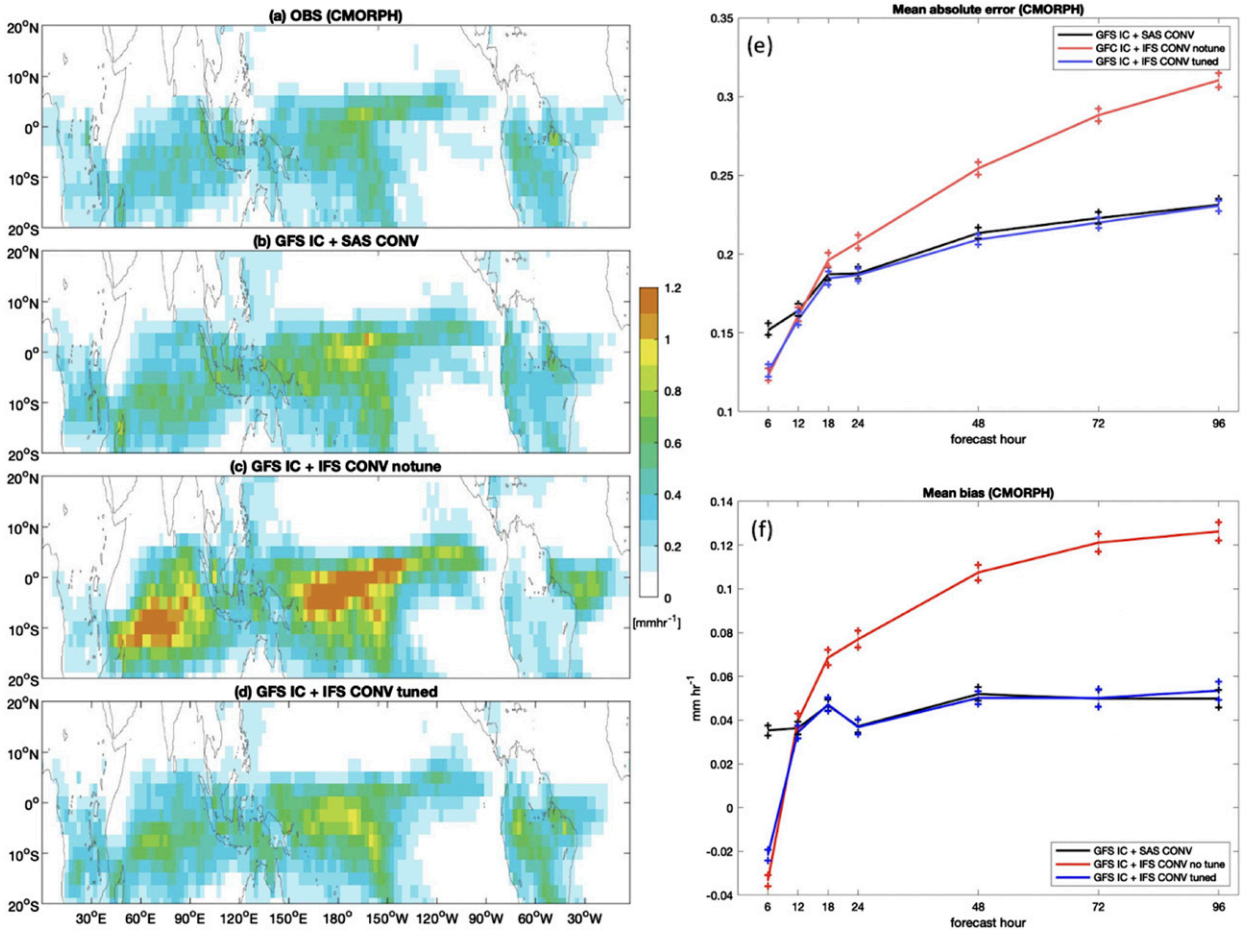

FIG. 1. Mean daily precipitation rate for the period January 2015–March 2016 from (a) CMOPRH observations and day-4 forecasts from (b) GFS IC–SASconv, (c) GFS IC–IFSconv notune, and (d) GFS IC–IFSconv. (e),(f) The mean absolute error and mean bias against CMORPH are shown, respectively, as a function of lead time. Vertical bars display the confidence interval of the estimated precipitation errors.

(deep, shallow, and midlevel), which shows a maximum drying extending from the surface to the top of the boundary layer, a secondary maximum of drying from roughly 900 to 600 hPa, then increasing to zero average tendency at about 250 hPa. Moistening from the PBL scheme (green curve) has a similar but opposite shape where the maximum occurs in the boundary layer, a secondary moistening layer occurs between 900 and 600 hPa, then decreasing to a zero-average tendency at about 500 hPa. It is interesting to compare these convection and PBL tendency profiles with those from the GFS model, which are represented by the solid blue (convection) and the solid green curve (PBL) in Fig. 2b. The most notable difference from the IFS model is that the maximum drying from the convection is elevated from the surface and occurs at about 850 hPa, with a corresponding equal and opposite moistening from the PBL scheme at the same level. If we now implement the IFS convection scheme as is, without any tuning, and without addressing interactions with any other physics schemes, the convection and PBL moisture tendency profiles behave as represented by the dashed blue and green curves in Fig. 2b. There is very little resemblance between these tendency profiles and those from the IFS model (Fig. 2a). The reasons for the differences in tendencies between the ECMWF and GFS-IFSconv are difficult to pinpoint. However, since the peak drying occurs within the PBL in the ECMWF along with the fact that the IFS shallow convection scheme uses the tendency from the PBL scheme as input, lead us to hypothesize that differences originate from feedbacks between the shallow convection and PBL schemes, as the GFS model with the SASAS scheme has an elevated peak drying at 925 hPa. To test this hypothesis, we replace the mass-flux profile that is locally computed following Siebesma et al. (2007) in the GFS models'

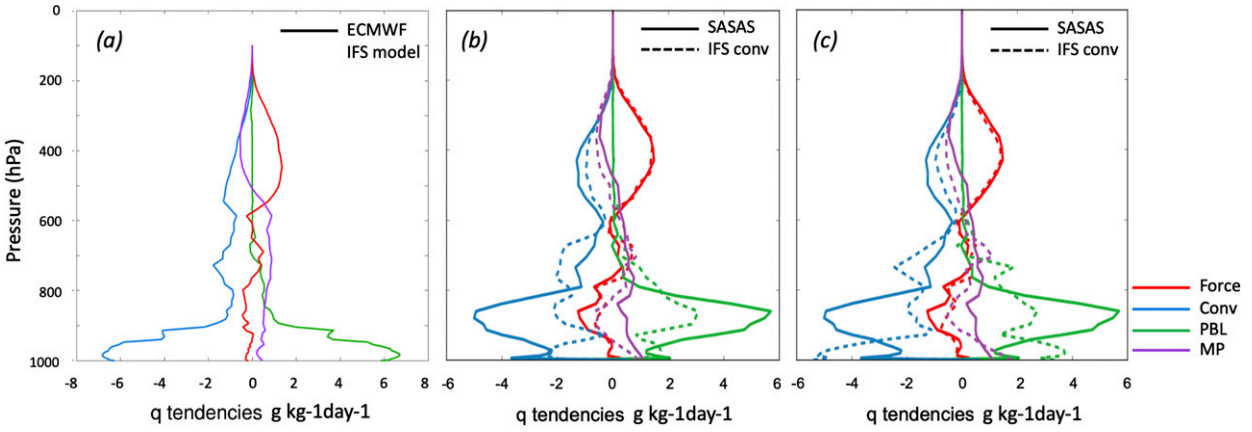

FIG. 2. Specific humidity tendency output for convection (blue), PBL (green), cloud microphysics (purple), and model forcing (red) for 1D simulations of the TWP-ICE campaign. Tendencies are averaged over the period 19 Jan–12 Feb 2016. (a) ECMWF IFS model output tendencies, (b) GFSIC-SASAS (solid) and "un-tuned" GFSIC-IFSconv (dashed) runs are shown. (c) GFSIC-SASAS (solid) and tuned GFSIC-IFSconv (dashed) runs are shown.

hybrid EDMF PBL scheme by the mass-flux from the IFS convection scheme, which yields the mass-flux component in unstable PBL regimes of the EDMF PBL scheme at the next time step. With this modification, the PBL scheme in convective regimes produces a more bottom-heavy moistening and this PBL tendency is then used as input to the convection scheme. The dashed blue and green curves in Fig. 2c demonstrate that this modification leads to convective profiles using the IFS scheme in GFS that resemble more closely those from the ECMWF IFS model.

2) INTERACTION WITH LARGE-SCALE CLOUD AND RADIATION SCHEMES

Along with the excess precipitation seen in Fig. 1c, the untuned 3D forecasts using the IFS cumulus convection introduced a model drift and bias related to excessive cloudiness. For instance, 3D forecasts with the untuned implementation of the IFS cumulus convection scheme showed a large increase in clouds seen by radiation (black curve in Fig. 3b). One reason for this increased cloud cover is the difference in cloud condensate detrainment profiles between the IFS convection scheme and the SASAS scheme. The area average detrainment profiles over the region 15°S to 15°N are shown in Fig. 3a. The black curve shows the detrained cloud condensation profile ($kg\,kg^{-1}$) of the untuned experiment, and shows that more cloud condensation is detrained compared with the SASAS scheme (red curve), particularly below 600 hPa, as the IFS convection scheme allows for cloud condensate (and mass) detrainment throughout the whole cloud layer. The cloud cover fraction in the GFS used for radiation computations in this version of the model is computed within the GFDL cloud microphysics package. Convective clouds contribute to the gridscale cloud condensate through cloud liquid and ice detrainment in the updraft. In Han et al. (2017) an update to the Xu and Randall (1999) cloud cover is implemented when using the SASAS convection scheme, where suspended cloud water in every cumulus layer is added to the gridscale cloud condensation for the cloud fraction and radiation computations. This was done to enhance cloudiness by the suspended cloud water in convective regions. In this version of the model (GFSv15.0.0), the cloud fraction is computed by the GFDL cloud microphysics scheme, which does not consider this addition of the suspended cloud water. However, the computation of the optical properties of the clouds seen by radiation still considers this update and adds convective suspended cloud water to enhance cloudiness. Thus, in our tuned version of the IFS convection scheme implementation, we remove this additional suspended convective cloud water and cloud ice.

Aside from the changes in the cloud optical properties seen by radiation, another update to the cumulus convection scheme that helps reduce the clouds seen by radiation is to increase the conversion from convective cloud condensate to convective precipitation. This modification results in less warming and drying by the IFS convection scheme throughout the troposphere, while further reducing the amount of detrained cloud condensate as well as a reduction of the cooling and moistening seen in the resolved cloud scheme. The large positive precipitation bias seen over the south-central Pacific Ocean (Fig. 1c) is particularly sensitive to these two modifications related to clouds seen by radiation and conversion rates.

The temperature and humidity tendencies averaged over 5-day forecasts initialized daily can be seen in

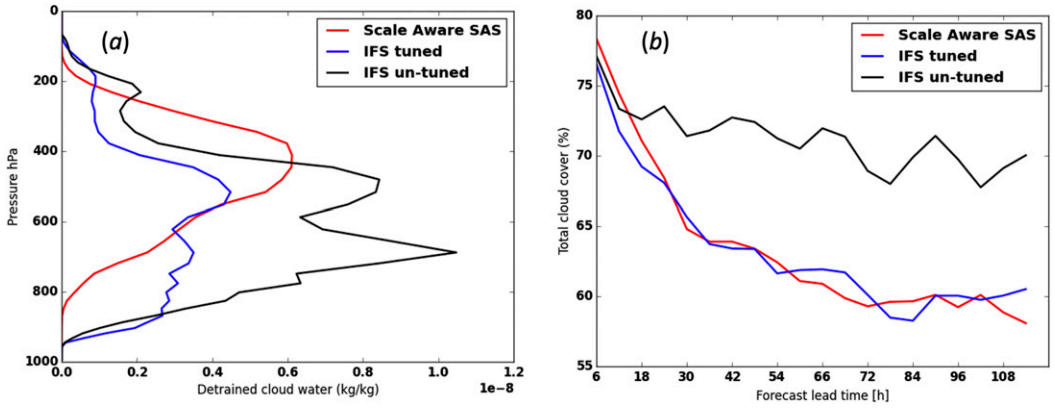

FIG. 3. (a) Detrained cloud condensate amount (kg kg^{-1}) over the area 15°S–15°N for the different configurations (see text for details) over the forecast period 1 Jan–31 Mar 2016. (b) Total cloud fraction (%) averaged over 15°S–15°N for the forecast period 1 Jan–31 Mar 2016.

Figs. 4a and 4d show the control run using GFS with the SASAS scheme, Figs. 4b and 4e show the untuned version of the FS cumulus convection scheme in GFS, and Figs. 4c and 4f show the version of the GFS model using the above described implementation adjustments. The tendencies are an average over the tropics from 15°S to 15°N. The 3D model tendencies averaged over the tropical belt are comparable to the ones found in the idealized TWP-ICE case discussed above. For example, the specific humidity tendency profiles from the convection and PBL schemes using the IFS convection are more bottom heavy compared to the GFS control run. The heating tendency profile from convection using the IFS convection scheme implies a stronger cooling tendency near the surface, and is shallower than the heating tendency profiles in the boundary layer seen in the SASAS scheme. This is also consistent with the temperature tendency output from the IFS model seen in the TWP-ICE case, and is likely due to more evaporation below the convective clouds in the IFS convection scheme compared with the SASAS scheme, and/or feedbacks associated with evaporation at the ocean surface.

From here on, we will use the tuned version of the IFS cumulus convection scheme in the GFS to look at the impact on CCEWs.

d. Initial conditions and replay methodology

In addition to the sensitivity to the cumulus convection parameterizations, here we also compare the relative impact of the initial conditions. A similar comparison between the relative impact of model physics and initial state within the NOAA FV3 GFS framework was recently made in Magnusson et al. (2019) and Chen et al. (2019), where a more general investigation of the midlatitude medium range forecast error (Magnusson et al. 2019) and tropical cyclone (Chen et al. 2019) forecast performance was conducted. Here we focus specifically on tropical variability, and the relative impact of the initial state versus the cumulus parameterizations on convectively coupled equatorial waves.

1) GFS INITIAL CONDITIONS

GFS initial conditions correspond to the analysis generated using the spectral GFS[1] dynamical core (GFS version 14.0.0, implemented in July 2017), which is regridded to the FV3 cubed-sphere grid. The initial conditions for the atmosphere, land surface and sea surface temperature (SST) used in this study come from a preoperational run for the January–March 2016 period, using a horizontal resolution of approximately 13 km at the equator, and 64 vertical levels. The spectral GFS analysis is obtained through the Global Data Assimilation System (GDAS), which uses a hybrid four-dimensional ensemble variational formulation ''hybrid 4DEnVar'' (Kleist and Ide 2015).

2) IFS INITIAL CONDITIONS

The ECMWF IFS initial conditions used in this study are based on the IFS model cycle 41r2, which became operational in March 2016, with 9 km resolution and 137 vertical levels. The data assimilation component of IFS consists of a four-dimensional variational data assimilation (4D-Var; Rabier et al. 2000) algorithm. The process of initializing with the IFS initial conditions starts with the model reading in the GFS initial conditions, and then overwriting winds, pressure, temperature and specific humidity from interpolated IFS data. The ability to

[1] Details about the spectral GFS model system can be found at https://vlab.ncep.noaa.gov/web/gfs/past-implementations.

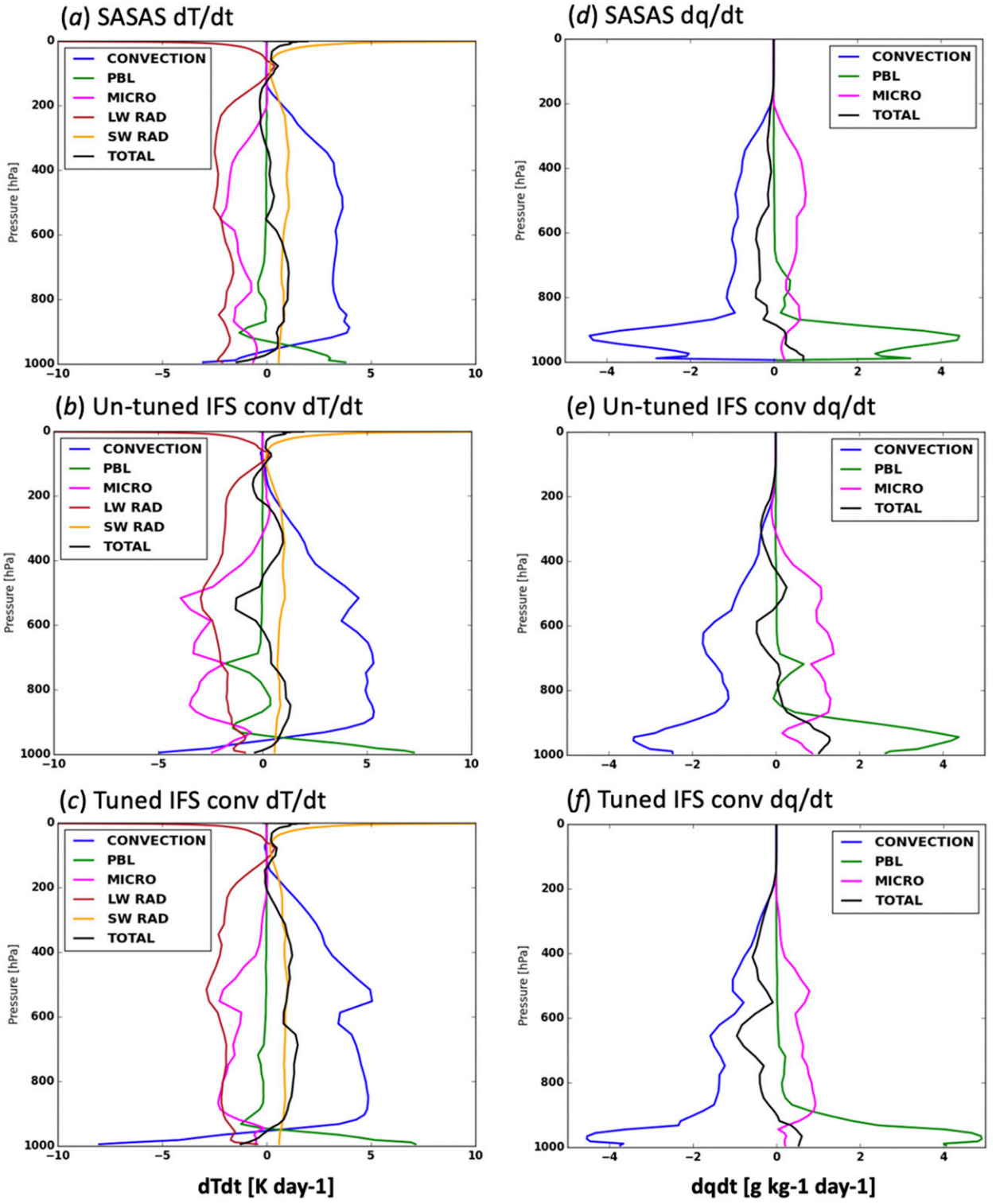

FIG. 4. Model tendency profiles for the different physical processes in the GFS model. (a)–(c) Temperature tendencies (K day^{-1}). (d)–(f) Specific humidity tendencies (g kg^{-1} day^{-1}). The tendencies are averaged over the latitude bands 15°S–15°N over all longitudes, and all forecast lead times during the period 1 Jan–31 Mar 2016.

TABLE 1. Summary of experiments setup.

Experiment	Initial conditions	Cumulus convection	Forecast length	Forecast period
Medium range forecasts:				
GFSIC-SASAS	GFS	SASAS	5 days	0000 UTC initializations everyday between 1 Jan and 1 Mar 2016
GFSIC-IFSconv	GFS	IFS conv	5 days	0000 UTC initializations everyday between 1 Jan and 31 Mar 2016
IFSIC-SASAS	IFS	SASAS	5 days	0000 UTC initializations everyday between 1 Jan and 31 Mar 2016
IFSIC-IFSconv	IFS	IFS conv	5 days	0000 UTC initializations everyday between 1 Jan and 31 Mar 2016
Seasonal forecasts:				
GFSIC-SASAS_long	GFS	SASAS	90 days	0000 UTC initializations every tenth day between 1 Dec and 21 Jan 2016
GFSIC-IFSconv_long	GFS	IFS conv	90 days	0000 UTC initializations every tenth day between 1 Dec and 21 Jan 2016
Replay forecasts:				
IFSIC-SASAS_replay	IFS	SASAS	6 h	Replayed forecasts nudged to the analysis every 6 h during the period 5 Jan–5 Mar 2016
IFSIC-IFSconv_replay	IFS	IFS conv	6 h	Replayed forecasts nudged to the analysis every 6 h during the period 5 Jan–5 Mar 2016

use the IFS initial conditions within FV3 in this study was made possible through an interpolation tool developed at NOAA GFDL to carefully interpolate from the IFS Gaussian grid to the cubed-sphere grid as documented in Chen et al. (2018), along with adjustments due to differences in the analyses' orography and vertical resolution.

3) REPLAY METHODOLOGY

"Replay" is a useful tool to constrain the model state with an analysis without running full data assimilation cycling. It was developed at NASA GMAO and described in detail in Orbe et al. (2017), with further stability refinements as described in Takacs et al. (2018). It leverages the 4D Incremental Analysis Update (4DIAU) capability of the data assimilation system, but skips the analysis step. Here we instead use precomputed analyses, in this case the IFS initial conditions described above. We replay to 6 hourly IFS analysis, which are interpolated offline to the GFS analysis (Gaussian) grid. A forecast from the previous analysis window is subtracted from the IFS analysis, which is called the analysis increment. The model is then backed up 3 h, the analysis increment is divided by the number of time steps over a 6-h window, and the model is run again across the 6-h window with these small increments of horizontal and meridional wind, temperature, humidity and pressure applied to the model physics tendencies each time step to bring the model closer to the observed trajectory. The forecast is continued across the next 6-h window with the forcing turned off. This new forecast is then used to compute the next analysis increment, and the process is repeated. The model's internal interpolation software converts from the Gaussian grid to the cubed-sphere grid. The IFS surface pressure is reduced to the FV3 orography, and level pressures are recomputed before vertical interpolation. In this study we use the replay methodology to study the analysis increments obtained from replaying the two different cumulus convection schemes to the IFS analysis every 6 h. A reduction of analysis increments using the IFS convection scheme in comparison to the SASAS convection scheme suggests that the model trajectory is able to stay closer to the IFS analysis.

3. Experiment setup

The various experiments, their initial conditions, cumulus convection schemes, forecast lead times and forecast time periods are listed in Table 1. All the experiments have a horizontal resolution of C384, which corresponds to roughly 25 km resolution, and 64 levels are used in the vertical.

4. Results

a. Seasonal runs

The purpose of the seasonal forecasts is to investigate if the GFSv15.0.0 can generate CCEW variability on its own (far away from its initial state), and whether the replacement of the cumulus parameterization schemes impacts the behavior of CCEWs. Common ways

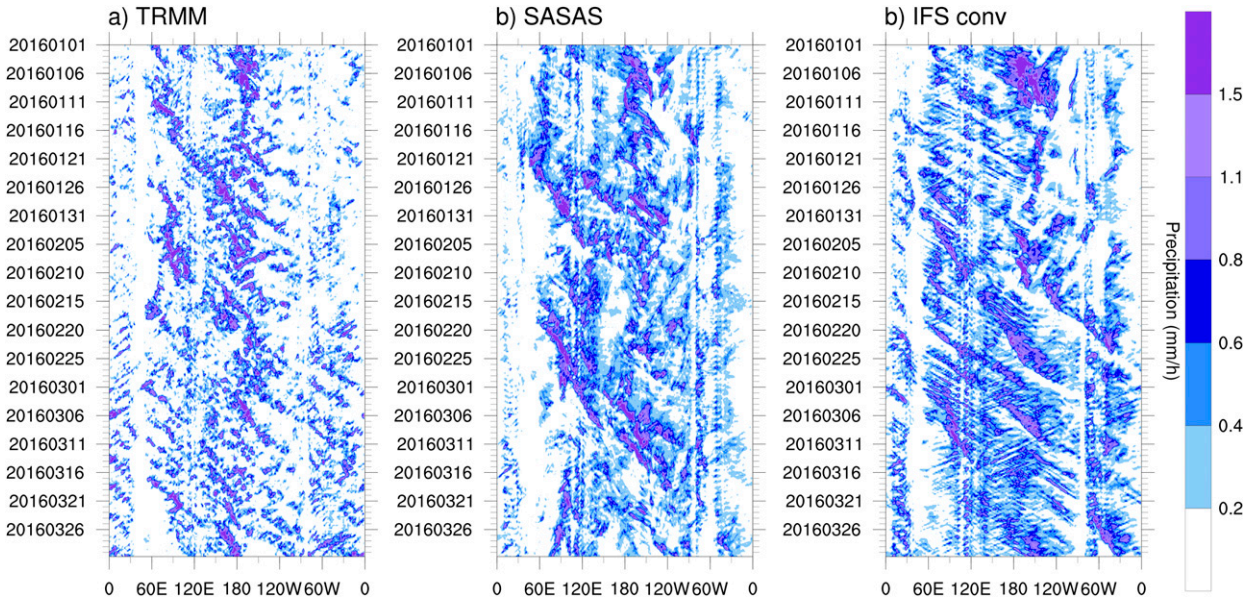

FIG. 5. Hovmöller diagram of 6-hourly precipitation initialized 1 Jan 2016 for (a) GPM product TRMM 3B42, (b) GFS with the SASAS scheme, and (c) GFS with the IFS convection scheme. The precipitation is averaged over the latitude bands 5°S–5°N.

of diagnosing CCEWs is through Hovmöller diagrams (Hovmöller 1949; Dole et al. 2018; Dias et al. 2018) and space–time power spectra (Wheeler and Kiladis 1999). The Hovmöller diagram in Fig. 5a illustrates how moderate to heavy observed precipitation in the tropics is organized by multiscale CCEWs, which appears as precipitating bands propagating to the east or to the west at various space–time scales. Especially prominent are the eastward propagating convectively coupled Kelvin waves (Kiladis et al. 2009). The Hovmöller diagrams in Figs. 5b and 5c shows 90-day forecasts of tropical precipitation over the same period, both initialized on 1 January 2016. These show that both model runs quickly deviate from the estimated precipitation field (Fig. 5a), and that both runs also have more light precipitation than the TRMM estimates. However, it should be noted that TRMM tends to underestimate very light precipitation amounts (Liu and Zipzer 2014) and the twice daily TRMM rates are an average over 3-hourly instantaneous rates as opposed to the model's 12-hourly average. Both models also feature a dominance of eastward propagation, particularly in the IFS convection run in Fig. 5c. It also appears that precipitation using the IFS convection scheme tends to have slightly higher amplitude than the SASAS scheme, in line with the results in Fig. 1.

Comparing Figs. 5b and 5c, it is clear that the IFS convection scheme impacts the character of the space–time organization of precipitation by promoting more organized zonally propagating features than the SASAS scheme. However, comparing the two modeled precipitation fields to observations, it is difficult to state whether one simulation is more realistic than the other without longer samples.

Comparing the model's mean state to TRMM and ERAI (Fig. 6) indicates that the implementation of the IFS convection scheme did not introduce any large model biases, but it is also not clear that the replacement of the convection scheme is associated with any substantial improvement in the mean tropical state. For instance, the pattern correlation analysis displayed in Table 2 implies a slight improvement over the global tropics and Indian Ocean when using the IFS convection scheme. However, in certain regions such as the eastern Pacific, the control run produces a better mean precipitation, even though the correlation in the divergence field is better using the IFS convection scheme, as indicated by the mean pattern correlation presented in Table 2.

In addition, the model-to-model mean pattern correlations presented in Table 2 suggests that there is a much stronger correlation between the model versions of divergence at 850 hPa, compared with divergence at 200 hPa, in all regions except the eastern Pacific (which is mainly dominated by lower level stratocumulus and large scale subsidence). This observation points to important differences in the two respective convection parameterizations in the tropical mid- and upper levels of the troposphere, such as differences in cloud depth. To understand this further, we investigate if this difference

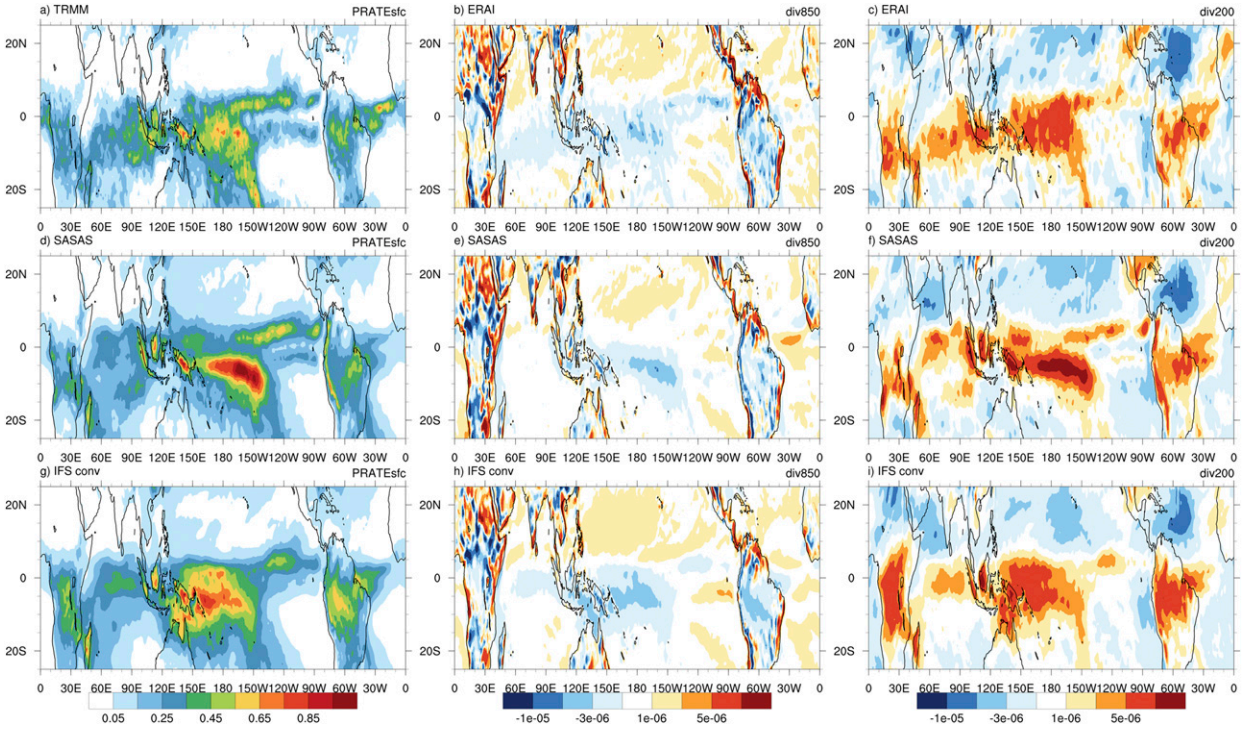

FIG. 6. Averages over the last 60 days of the 90 day forecasts for the tropical belt 25°S–25°N. (left) Precipitation for (a) TRMM, (d) GFSIC-SASAS_long experiment, and (g) GFSIC-IFSconv_long experiment; (middle) 850 hPa mean divergence for (b) ERAI, (e) GFSIC-SASAS_long experiment, and (h) GFSIC-IFSconv_long experiment; (right) 200 hPa divergence for (c) ERAI, (f) GFSIC-SASAS_long experiment, and (i) GFSIC-IFSconv_long experiment.

may be attributed to the difference in active (deep) and suppressed (shallow and midlevel) convective modes.

To compare how often the respective convection schemes call deep, shallow, or midlevel (elevated) convection, we compute the accumulated number of times a grid point is defined as a deep convective, shallow convective or a midlevel convective point within a 6-h time window. As we are using a model time step of 450 s, it means that the maximum times a grid point can be classified as convective in a 6-h period is 48 times. Figure 7a show the time mean (over all the full 90 day simulations) accumulated points over a 6-h time window that are classified as deep convective. As can be seen, the IFS cumulus convection scheme triggers deep convection much more frequently than the SASAS convection scheme, both temporally and spatially. In fact, many grid points in the Pacific and Indian Ocean trigger deep convection every time step in the IFS cumulus convection scheme, and as a mean over the period almost twice as often. The same comparison for triggered shallow convective points can be found in Fig. 7b. Here, instead, the SASAS scheme calls shallow convection more frequently compared with the IFS convection scheme, although the areal distribution of where shallow convection is triggered is similar in the two schemes. Over land, it appears that the IFS convection scheme triggers

TABLE 2. Pattern correlation coefficients for the maps shown in Fig. 6. Pattern correlations are computed for the longitude regions indicated by the table header, all between 15°S and 15°N. The differences in correlation between SASAS and observations and IFS convection and observations that are statistically significant at the 90% level based on a *t* test are shown in bold font. Observations/reanalysis used are TRMM for precipitation and ERAI for divergence.

	Tropical Belt (0°–360°E)			Indian Ocean (45°–90°E)			West Pacific (150°–210°E)			East Pacific (240°–275°E)		
	OBS–SASAS	OBS–IFSconv	SASAS–IFSconv	OBS–SASAS	OBS–IFSconv	SASAS–IFSconv	OBS–SASAS	OBS–IFSconv	SASAS–IFSconv	OBS–SASAS	OBS–IFSconv	SASAS–IFSconv
P	**0.60**	**0.63**	0.67	**0.44**	**0.56**	0.72	0.62	0.58	0.62	0.63	0.58	0.73
D850	**0.51**	**0.56**	0.76	**0.52**	**0.57**	0.78	**0.65**	**0.67**	0.65	**−0.05**	**0.33**	0.3
D200	**0.56**	**0.62**	0.57	**0.40**	**0.57**	0.61	0.61	0.60	0.58	**0.35**	**0.46**	0.40

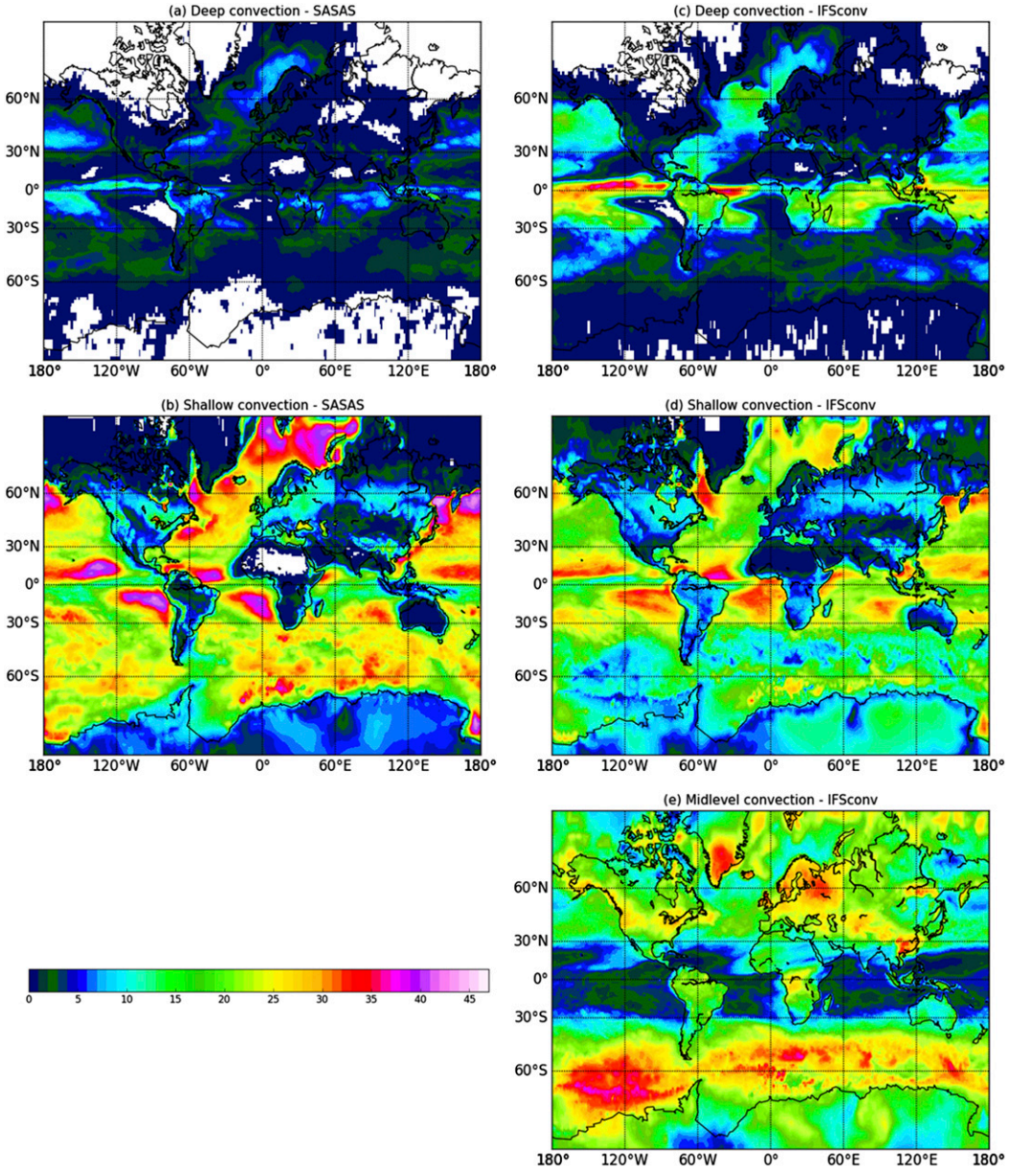

FIG. 7. Accumulated number of times a convective type is called within a 6-h time period, averaged over all the 90-day seasonal forecast runs. (a) SASAS deep convection, (b) SASAS shallow convection, (c) IFS deep convection, (d) IFS shallow convection, and (e) IFS midlevel (elevated) convection.

shallow convection more often, particularly over South America. The elevated convection triggered by the IFS convection scheme is shown in Fig. 7c. This convection type is triggered if neither deep convection nor shallow convection has been found. As summarized in IFS cy45r1 documentation; Browning et al. (1973) and Herzegh and Hobbs (1980) have shown that elevated convection occurs in warm fronts, and in the warm sector of extratropical cyclones, and that the main source of moisture comes from low-level convergence (Houze et al. 1976). The IFS convection scheme is developed to parameterize such elevated convection based on the diagnostic studies mentioned above (IFS cy45r1 documentation). It is assumed that midlevel convection can be activated between 0 and 10 000 m in association with moist air and large-scale ascent. The closure of this type is the only place in the IFS convection scheme where the convection is directly linked to the gridscale velocity field. While this convection type seems to explain some of the coherence between

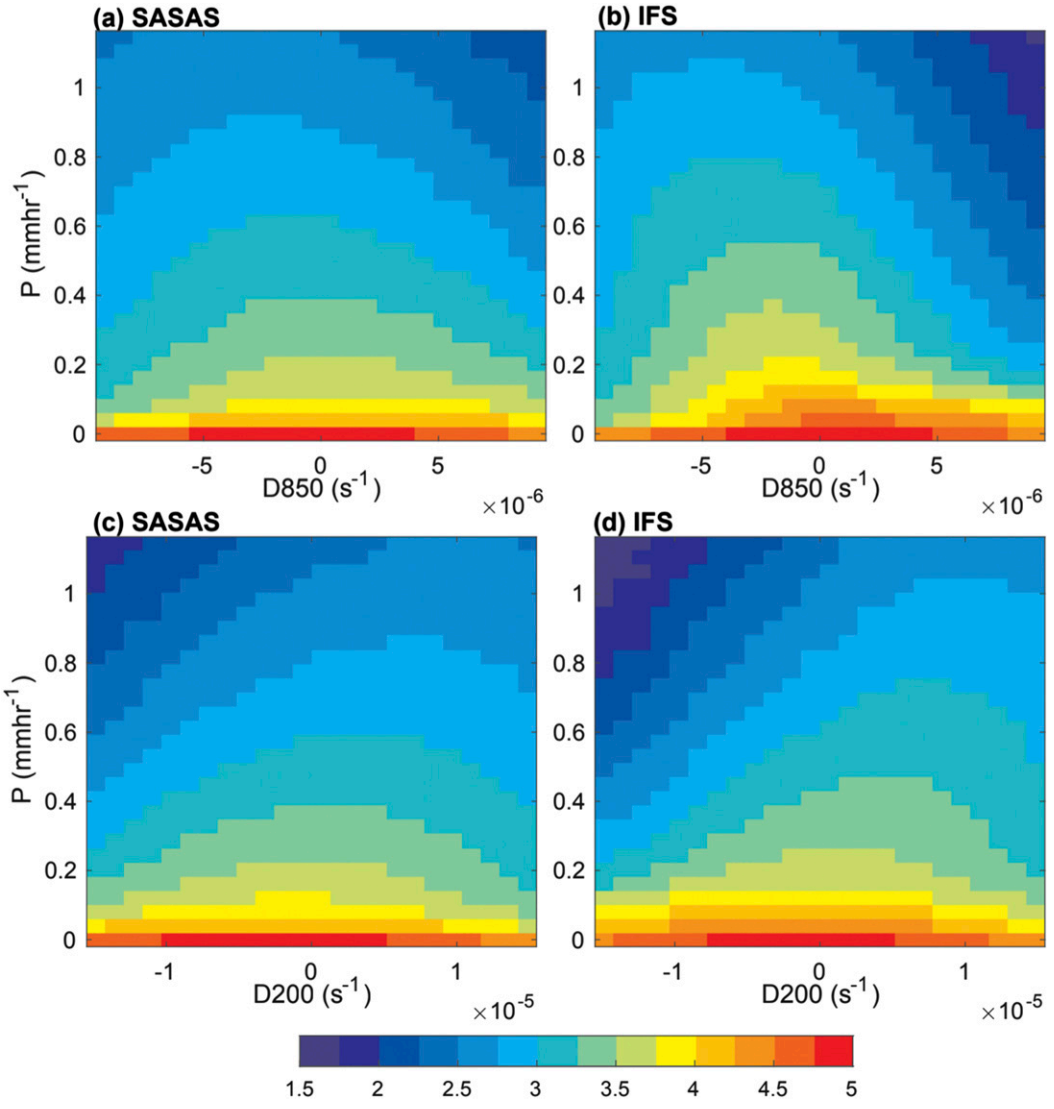

FIG. 8. Two-dimensional histograms of daily (top) 850 hPa divergence and precipitation and (bottom) 200 hPa divergence and precipitation. (a),(c) GFSIC-SASAS_long experiment and (b),(d) GFSIC-IFSconv_long experiment. The histograms include all precipitating data points between 15°S and 15°N. Shading represents the log10 of the number of data points in each bin. Twenty-five bins were used along each axis where the range displayed includes 90% of all data points.

low-level convergence and precipitation in theory, in practice midlevel convection in the IFS convection scheme is often activated in moist layers near the top of the boundary layer if no shallow convection is found (IFS cy45r1 documentation), which seems to be consistent with the finding in Fig. 7c. Looking at the mean divergence maps in Fig. 6, it appears that it is mainly the more frequent triggering of deep convection in the IFS convection compared with the triggering of deep convection in the SASAS scheme that is generating a stronger coherence between upward motion in the lower troposphere and precipitation.

In addition to the mean divergence and precipitation fields, we also look at the frequency distribution of these fields, and their correlation (Fig. 8) to understand if the tropical variability is also impacted by the convection scheme. Comparing Figs. 8a and 8b, the distribution of low-level divergence becomes more left-skewed at higher rain rates when using the IFS convection scheme. In other words, stronger low-level inflow is more tightly associated with stronger rain rates with the IFS convection scheme. Similarly, comparison between Figs. 8c and 8d, suggests a stronger relationship between upper-level outflow and precipitation when using the IFS convection scheme.

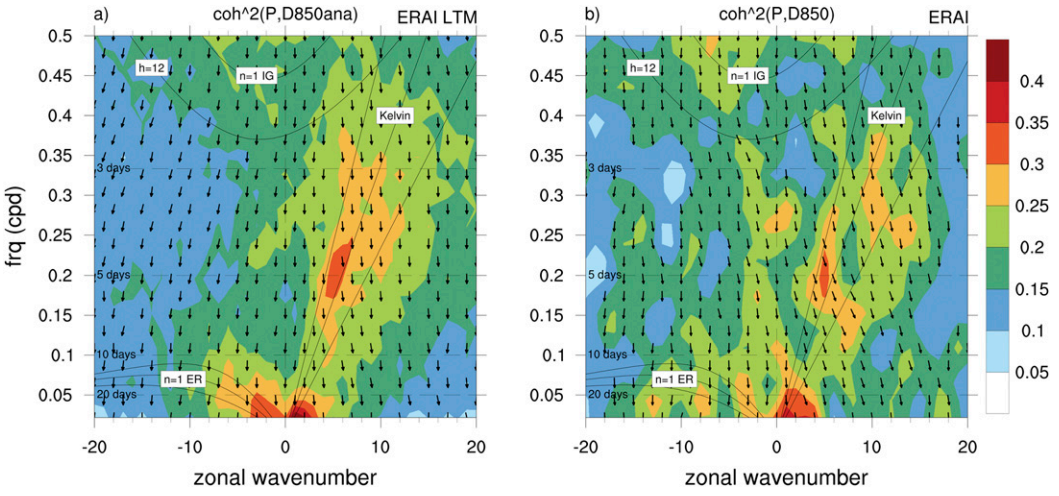

FIG. 9. Frequency–wavenumber coherence-squared spectra averaged from 15°S to 15°N between 850 hPa divergence and precipitation for (a) ERAI JFM long term mean, and (b) ERAI valid at the same dates as the 90 day forecasts (see text for details). Phase angles are shown where the coherence-squared is significant at the 95% level. Dispersion curves shown are for equatorial waves as in Wheeler and Kiladis (1999), for equivalent depths of 12, 25, and 50 m.

Interestingly, the differences in upper-level divergence between the GFS in its standard configuration and with the IFS convection scheme suggest a potential for remote impacts associated with the change in convective schemes because the upper-level divergent circulation is known to be a source of Rossby waves that propagate to the extratropics impacting weather downstream (Sardeshmukh and Hoskins 1988; Branstator 2014). Taken together, Figs. 5, 6, and 8 imply that the space–time organization of tropical variability is more strongly affected by the change in the convection scheme than the mean state is. This is an important point because it suggests that the enhancement of large-scale space–time convective organization seen with the IFS convection scheme is not necessarily due to a change in the mean state that disturbances are embedded in.

The next question we need to address is whether the organized precipitating features seen in Fig. 5c are realistic, even though they might not be occurring at the correct time or location. In other words, we are interested in the question of whether the replacement of the convection scheme leads to an improvement in the model's ability to generate and propagate CCEWs. For this purpose, we draw on the full ensemble of runs every 10 days. To test if the zonally propagating features seen with the IFS convection scheme is spurious or not, we analyze the space–time coherence spectra between precipitation and low-level divergence, which is another standard diagnostic of tropical variability. To calculate the coherence spectra, we follow the methodology from Dias et al. (2018). First, each 90-day forecast is split into 46-day segments overlapping by 20 days. Longitude–time cross spectra are computed for each segment and at each latitude from 15°S to 15°N and then averaged over latitude, segments and all 90 day runs. The resulting averaged power, quadrature and cospectra are used to compute the coherence-squared and phase spectra (Wheeler and Kiladis 1999; Hendon and Wheeler 2008). For the long-term mean ERAI coherence spectra, the same methodology is applied to each January–March and the cross spectra are averaged across all years from 1979 to 2018 before the coherence-squared and phase spectra are computed. To estimate the impact of sampling on the coherence and phase we also compute the ERAI spectra for the same dates as the 90-day forecasts.

The long-term mean (January–March 1979–2018) ERAI coherence-squared and phase spectra between ERAI precipitation and 850 hPa divergence (Fig. 9a) show that, in the reanalysis, regions of high coherence-squared tend to match up with the MJO and with Matsuno's equatorial wave dispersion curves (Matsuno 1966) for equatorial Rossby waves, inertio-gravity waves, and Kelvin waves. Phase arrows pointing downward and slightly rightward indicate that low-level convergence leads precipitation in ERAI. Note that when using TRMM estimates of precipitation instead of ERAI precipitation the coherence levels decrease and the phase relationship changes to ERAI low-level convergence leading TRMM precipitation by 1/8 of a cycle (not shown). Dias et al. (2018) also show that the ECMWF IFS model has an overall better representation of the coherence and phase than the GFS model has. For the 90-day sampled ERAI (Fig. 7b) the coherence-squared is not as prominent as in the long-term mean,

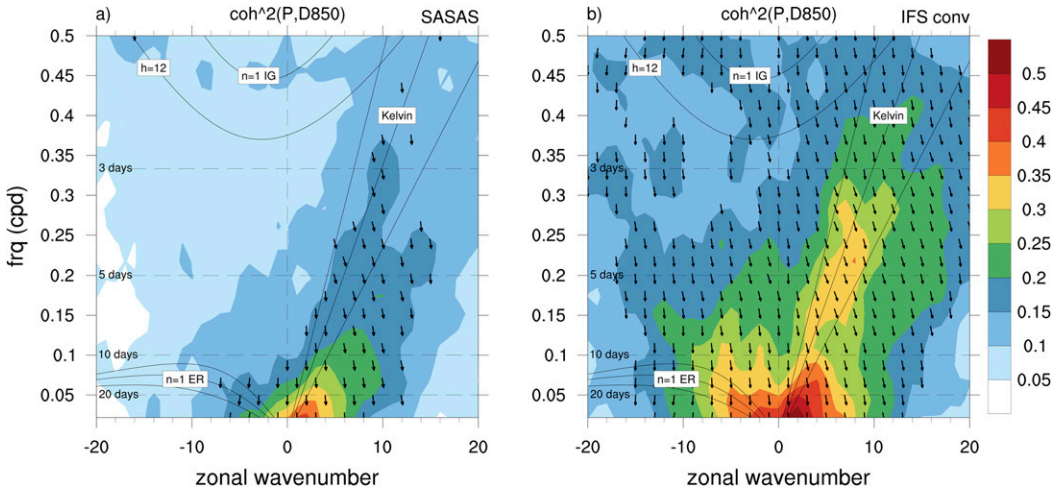

FIG. 10. As in Fig. 9, but for GFS runs with (a) SASAS convection scheme and (b) IFS convection scheme.

although there is some enhancement of coherence along the Kelvin wave, MJO, and ER bands even though the sample is small. Figure 10 shows that the IFS convection scheme in the GFS model (Fig. 10b) is more coherent along CCEW than the GFS with the SASAS scheme (Fig. 10a), especially along the Kelvin wave dispersion curve. Despite the relatively short simulations, it is interesting that there is also some evidence of improvement along the MJO band. Note that, if the goal is to match the modeled coherence patterns with reanalysis, then the IFS convection scheme represents a step in the right direction. These results, along with the Hovmöller diagrams discussed above, demonstrate that the IFS convection scheme in the GFS model has a noticeable impact on how the large-scale flow couples to precipitation, and seems to favor space–time convective organization in a more realistic way.

b. *Medium-range forecasts and sensitivity to initial conditions*

Next, we investigate the impact that the respective cumulus schemes have on CCEWs in medium range weather forecasts, and compare this to the impact seen by interchanging the initial conditions of the model. Figure 11 shows the symmetric component of the forecast precipitation power spectra applied at 6- and 60-h lead time (second and third rows), and two sets of observations (TRMM and CMORPH) matching the forecast valid times displayed in the top panels. At forecast hour 6 (left two columns), initialization with the IFS analysis leads to a precipitation spectrum that is closer to observations with either convective scheme (Figs. 11i,j). In particular, in IFSIC-SASconv and IFSIC-IFSconv power along the Kelvin wave dispersion curve extends to higher frequencies as in the observations (positive wavenumbers and periods between 2 and 6 days), which is in contrast to the power spectra from GFSIC-SASconv and GFSIC-IFSconv (Figs. 11e,f). This difference implies that the IFS initial conditions in the tropics are better than in the GFS, which could be due to a combination of higher horizontal and vertical model resolution, seemingly better physical parameterizations in the tropics, as well as better use of observations. At forecast hour 60, the spectra in all of the model runs display more power at low frequencies and wavenumbers than in the observations, but in general the runs using the IFS convection scheme continue to show more power along the Kelvin mode. The enhanced power along the Kelvin wave dispersion curve suggests that when the model is initialized with a Kelvin wave type of disturbance, the modified model configuration is able to propagate it for longer lead times than with the standard physics. Because we are analyzing a relatively short period (3 months) it is difficult to assess the impact of the convection scheme on the MJO, but at least all the spectra do maintain an MJO peak to varying degrees.

Figure 12 shows the bias, mean absolute error, and pattern correlation of the 6-h average model precipitation and TRMM observations averaged over all daily initializations for the entire 3 month period. Interestingly, initializing the model with IFS initial conditions (gray and red lines), gives the best precipitation bias and maintains an improved pattern correlation throughout the model forecast, compared with initializing the model with GFS initial conditions (black and blue lines). This improvement in pattern correlation seen from initializing with the IFS initial conditions is also superior to the improvement when only replacing the cumulus convection scheme with the IFS scheme (blue lines). The improved

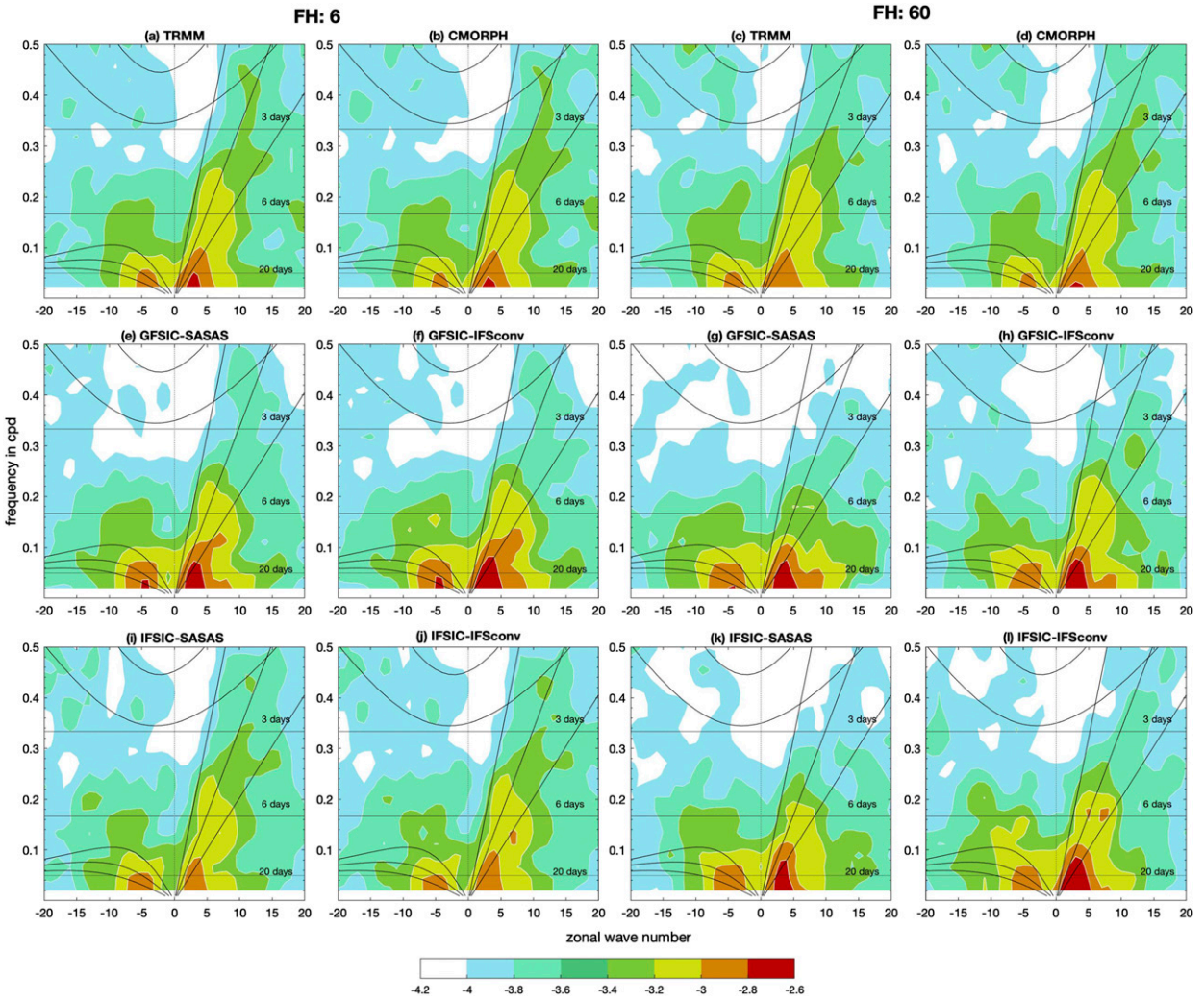

FIG. 11. Zonal wavenumber and frequency power spectra (log10 of the power) of symmetric rain rates about the equator averaged from 15°S to 15°N of (a),(c) TRMM, (b),(d) CMORPH, (e),(g) GFSIC-SASconv, (f),(h) GFSIC-IFSconv, (i),(k) IFSIC-SASconv, and (j),(l) IFSIC-IFSconv. Forecast hour 6 (60) is displayed on the left (right) two columns with 6 hourly time intervals and valid times from 0600 UTC 1 Jan to 0600 UTC 30 Mar 2016 (1200 UTC 3 Jan to 1200 UTC 2 Apr 2016). (top) Observations match the (bottom),(middle) forecast valid times.

precipitation pattern correlation throughout the entire forecast period suggests that deficiencies in the model initialization have a negative impact on the forecast precipitation out to at least 4 days. Notice also that most of the vertical error bars overlap with one another, so while differences seem systematic across lead times, they are relatively small and not always significant.

Another interesting point is that, given the same GFS initial conditions, the run with the IFS convection scheme yields a better pattern correlation, and improved mean absolute error compared with using the SASAS convection scheme. However, given the same IFS initial conditions, the SASAS convection scheme actually provides the best pattern correlation and mean absolute error of all forecasts after forecast hour 18. In the mean bias plot we see a large negative bias at forecast hour 6 when using the IFS convection scheme and starting from GFS initial conditions. Similarly, there is a very large positive bias at forecast hour 6 when using the SASAS scheme, and starting from the IFS initial conditions. This suggests that the IFS initial conditions are moister than the GFS initial conditions, consistent with findings discussed in the next section, which results in large spinup and spindown of precipitation during the first 6 h of the forecast.

c. *Replay runs*

By replaying the forecasts with the two different convection schemes to the IFS initial conditions, we can compare the analysis increments (in this case

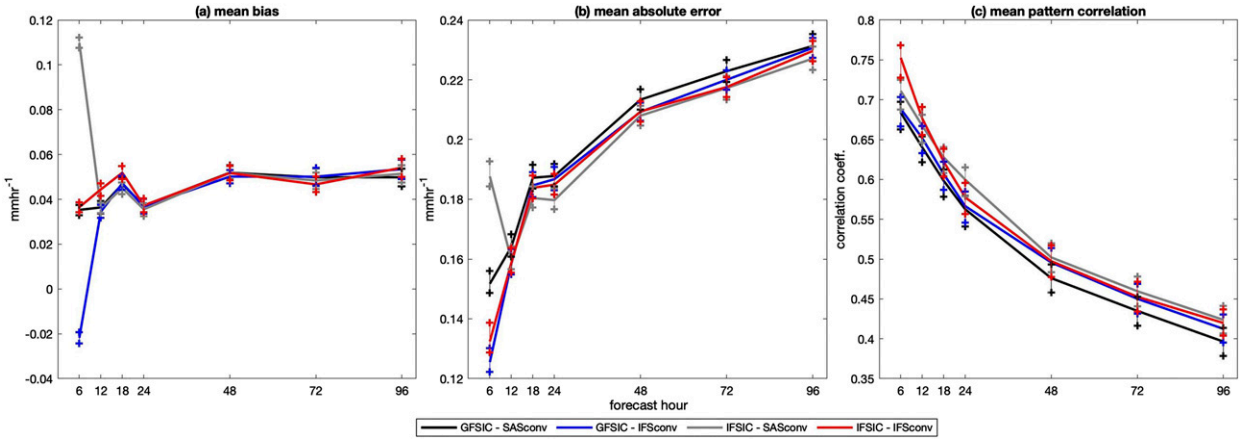

FIG. 12. Display of precipitation forecast (a) bias, (b) mean absolute error, and (c) 15°S–15°N mean pattern correlation. Vertical lines display the confidence interval of each estimate (details in section 4b).

the analysis minus the first guess forecast) to get a sense of how close we are to the IFS analysis between the two. The analysis increments of temperature and humidity are presented in Fig. 13. These are the average increments for the period 5 January–5 March 2016, over the latitude band 15°S–15°N. Here the red colors indicate that the analysis is warmer/moister than the first guess forecast, and similarly blue colors indicate that the analysis is colder/drier than the first guess forecast. Over this domain, the simulations show that the SASAS scheme yields a lower troposphere that is warmer than the analysis, whereas the IFS convection scheme gives a slightly cooler lower troposphere compared with the analysis. Both model simulations (with the two different convection schemes) are drier than the analysis in the lower PBL compared with the ECMWF IFS analysis. Between model level 10 and 20 (~925–850 hPa) there is a layer that is drier with the SASAS scheme (compared with the IFS analysis), that switches sign upon implementation of the IFS convection scheme. This is consistent with the change seen in the humidity tendencies (Fig. 4) between the SASAS scheme and the IFS convection scheme, where drying from the convection scheme is present between 925 and 850 hPa in the SASAS scheme.

Between the surface and ~925 hPa (model level 10), the analysis is moister than the first guess forecast with both convection schemes. We made several attempts at tuning the IFS convection scheme to make it moister within the PBL, including increasing the evaporation from convective precipitation and increasing the convective rain. However, the analysis humidity increments at the lowest levels showed very little sensitivity to changes in the convection scheme (not shown). We also tried evaporating more rain in the GFDL cloud microphysics scheme, which did not result in any significant change in the PBL moisture (not shown).

The reason why the ECMWF IFS analysis is moister compared with the forecasts in the above described replay experiments may be attributed to the fact that there are differences in the use of humidity observations entering the ECMWF IFS data assimilation, or the IFS model background (first guess) forecast used in the data assimilation is itself moister than the GFS forecast model. To understand this further, we look at the analysis increments from the two respective operational model systems (for the GFS this is the preoperational parallel for GFS v.15; Fig. 14), as an average over 15°S–15°N. The analysis increments are averaged over all 0000 and 1200 UTC initial times for the period 1 January–28 February 2016. Figure 14a shows that the analysis increments in the ECMWF IFS system are negative in the lower troposphere, indicating that the analysis is working to dry the tropical lower troposphere where the first guess forecast is too moist. Figure 14b shows a generally opposite behavior in the GFS system, where the analysis increments look to be more positive (or less negative) in the lower tropical troposphere compared with the ECMWF IFS model. The analysis increments are positive over the eastern and western Pacific and the Maritime Continent, indicating that the analysis is trying to moisten this region where the model tends to be too dry. This means that the ECMWF IFS model itself acts to moisten the lower tropical troposphere, where the GFS model acts to dry. This explains, at least partly, why the analysis increments obtained by replaying to IFS analyses are positive in the lower troposphere when using the GFS model physics in its default configuration. As seen in Fig. 13, replacing the GFS SASAS convection scheme with IFS convection scheme is not sufficient to produce a background forecast that is as moist in the lower PBL as the IFS model. This suggests that other aspects of the IFS

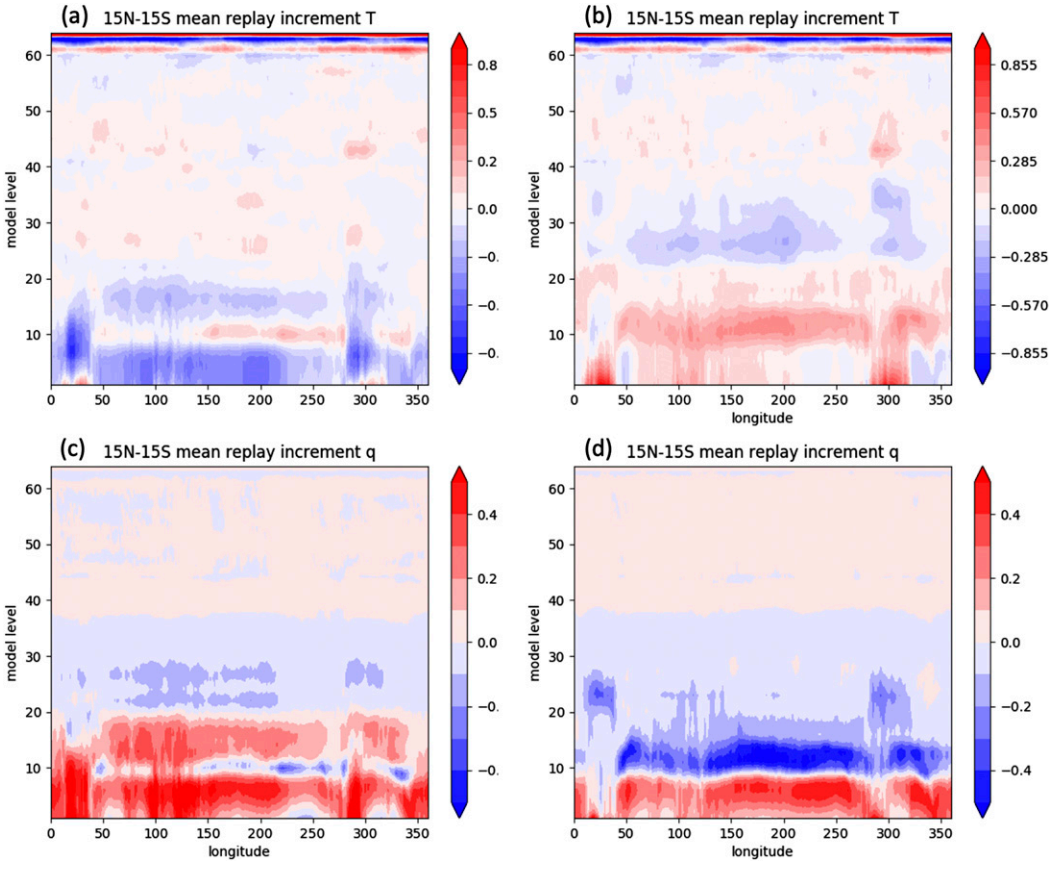

FIG. 13. Time and latitudinally average replay increments for (a) SASAS T-increment, (b) IFS convection T-increment, (c) SASAS q-increment, and (d) IFS convection q-increment. All fields are averaged from 0000 UTC 5 Jan to 0000 UTC 5 Mar 2016 and from 15°N to 15°S. Red areas indicate where the IFS analyses are moister or warmer than the short-range forecasts. See section 2d for more details on the replay methodology and experimental design.

physics are contributing to this difference, such as differences in PBL physics, surface fluxes and cloud and precipitation microphysics.

Furthermore, compared with soundings over the tropics, model simulations with the IFS convection scheme yield a moister PBL after 3–5 days into the forecast, whereas simulations with the SASAS scheme have a dry bias in the PBL (not shown). Similarly, model runs using IFS initial conditions start off with a moister PBL than runs with GFS initial conditions (not shown). This difference is interesting, as shown in previous studies (e.g., Mapes et al. 2006), this added moisture in the PBL can also contribute to more realistic transitions from shallow to deep convection, and, therefore, to better representation of CCEWs.

5. Conclusions

In this study we implemented the cumulus convection schemes from IFS cy45r1 into a research version of GFSv15.0.0 with the aim to understand whether the IFS convection scheme is able to improve GFS simulations of tropical variability and large-scale convective organization, and how the characteristics of the heating and moistening profiles in GFS are changed upon this implementation. The following points represent our main findings:

- The budget analysis done in this study shows that the GFS PBL tendencies are surprisingly strong, with a minimum at the surface. The reason for such a behavior in the PBL scheme should be investigated further in the future.
- The IFS models' tropical convective temperature and humidity tendency profiles are very different from the profiles found in the GFS model in the lower troposphere. In GFS there is a strong drying from convection at 925 hPa that is not present in the IFS model. We show that a consistent treatment of the interaction between parameterized convective plumes in the GFS

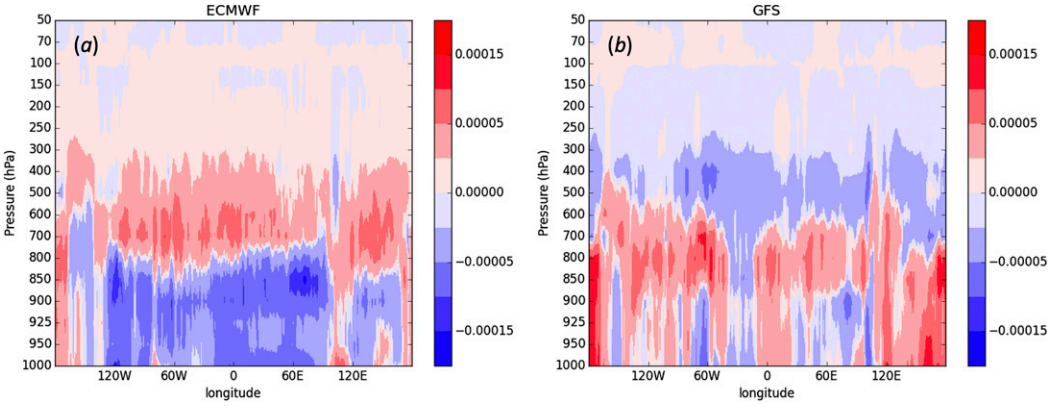

FIG. 14. Time and latitudinally averaged specific humidity (kg kg^{-1}) analysis increments from the (a) ECMWF IFS operational model and (b) NOAA NCEP GFS operational model. The analysis increments are computed as the analysis minus the first guess forecast 6 h prior to the analysis, averaged over all 0000 and 1200 UTC initializations between 1 Jan and 28 Feb 2016, between 15°S and 15°N.

PBL and the IFS convection scheme in the GFS model physics, is required in order to replicate (in the GFS) the tropical temperature and moisture profiles that are simulated by the IFS model.

- Given the necessary adjustments to the IFS convection scheme in the GFS, so that it replicates the tendencies of the ECMWF model, improved convective organization and a tendency to propagate disturbances is obtained with the GFS compared to its operational version.
- The IFS convection scheme shows more coherence between low-level convergence and surface precipitation. There is also a stronger model-to-model correlation of low-level divergence at 850 hPa compared with upper-level divergence at 200 hPa between the two model versions, pointing to differences in the cumulus parameterizations at mid- to upper levels of the troposphere. One possible reason for this can be attributed to the frequency difference in triggering of active and suppressed convective modes, where the IFS convection scheme tends to trigger deep convection much more frequently than the SASAS scheme in the tropics.
- The operational ECMWF IFS model acts to moisten the lower tropical troposphere to a larger extent than the operational GFS model, which can only be partly attributed to their convection scheme. As shown in previous studies (e.g., Mapes et al. 2006), this added moisture in the PBL can also contribute to more realistic transitions from shallow to deep convection, and, therefore, to better representation of CCEWs.

This study is in general agreement with previous literature indicating that CCEWs are highly sensitive to the convection scheme as well as feedback with other physical parameterizations. Therefore, improvement of NOAA's weather to climate predictions in the tropics, as well as their global impacts, strongly rely on further development of physics related to clouds and precipitation. We hope that this study will both motivate and provide guidance for such improvements.

Acknowledgments. This research was partially supported by the Physical Science Division of NOAA's Earth System Research Laboratory, and by the California Department for Water Resources (CDWR). The authors thank two anonymous reviewers for their insightful comments that helped improve this manuscript.

REFERENCES

Arakawa, A., and W. H. Schubert, 1974: Interaction of a cumulus cloud ensemble with the large-scale environment. Part I. *J. Atmos. Sci.*, **31**, 674–701, https://doi.org/10.1175/1520-0469(1974)031<0674:IOACCE>2.0.CO;2.

Bassill, N. P., 2015: An analysis of the operational GFS simplified Arakawa Schubert parameterization within a WRF framework: A Hurricane Sandy (2012) long-term track forecast perspective. *J. Geophys. Res. Atmos.*, **120**, 378–398, https://doi.org/10.1002/2014JD022211.

Bechtold, P., M. Kohler, T. Jung, M. Leutbecher, M. Rodwell, F. Vitart, and G. Balsamo, 2008: Advances in predicting atmospheric variability with the ECMWF model, 2008: From synoptic to decadal time-scales. *Quart. J. Roy. Meteor. Soc.*, **134**, 1337–1351, https://doi.org/10.1002/qj.289.

——, N. Semane, P. Lopez, J.-P. Chaboureau, A. Beljaars, and N. Bormann, 2014: Representing equilibrium and non-equilibrium convection in large-scale models. *J. Atmos. Sci.*, **71**, 734–753, https://doi.org/10.1175/JAS-D-13-0163.1.

Branstator, G., 2014: Long-lived response of the midlatitude circulation and storm tracks to pulses of tropical heating. *J. Climate*, **27**, 8809–8826, https://doi.org/10.1175/JCLI-D-14-00312.1.

Browning, K. A., M. E. Hardman, T. W. Harrold, and C. W. Pardoe, 1973: The structure of rainbands within a mid-latitude depression. *Quart. J. Roy. Meteor. Soc.*, **99**, 215–231, https://doi.org/10.1002/qj.49709942002.

Chen, J.-H., and S.-J. Lin, 2011: The remarkable predictability of inter-annual variability of Atlantic hurricanes during the past decade. *Geophys. Res. Lett.*, **38**, L11804, https://doi.org/10.1029/2011GL047629.

——, and ——, 2013: Seasonal predictions of tropical cyclones using a 25-km-resolution general circulation model. *J. Climate*, **26**, 380–398, https://doi.org/10.1175/JCLI-D-12-00061.1.

——, X. Chen, S.-J. Lin, L. Magnusson, M. Bender, L. Zhou, and S. Rees, 2018: Tropical cyclones in GFDL fvGFS – Impacts of dycore, physics and initial conditions. *33rd Conf. on Hurricane and Tropical Meteorology*, Ponte Vedra, FL, Amer. Meteor. Soc., 9B.4, https://ams.confex.com/ams/33HURRICANE/webprogram/Paper339827.html.

——, and Coauthors, 2019: Advancements in hurricane prediction with NOAA's next-generation forecast system. *Geophys. Res. Lett.*, **46**, 4495–4501, https://doi.org/10.1029/2019GL082410.

Chikira, M., and M. Sugiyama, 2013: Eastward-propagating intraseasonal oscillation represented by Chikira–Sugiyama cumulus parameterization. Part I: Comparison with observation and reanalysis. *J. Atmos. Sci.*, **70**, 3920–3939, https://doi.org/10.1175/JAS-D-13-034.1.

Davies, L., and Coauthors, 2013: A single-column model ensemble approach applied to the TWP-ICE experiment. *J. Geophys. Res. Atmos.*, **118**, 6544–6563, https://doi.org/10.1002/jgrd.50450.

Dee, D. P., and Coauthors, 2011a: The ERA-Interim reanalysis: Configuration and performance of the data assimilation system. *Quart. J. Roy. Meteor. Soc.*, **137**, 553–597, https://doi.org/10.1002/qj.828.

Dias, J., M. Gehne, G. N. Kiladis, N. Sakaeda, P. Bechtold, and T. Haiden, 2018: Equatorial waves and the skill of NCEP and ECMWF numerical weather prediction systems. *Mon. Wea. Rev.*, **146**, 1763–1784, https://doi.org/10.1175/MWR-D-17-0362.1.

Dole, R., and Coauthors, 2018: Advancing science and services during the 2015/16 El Niño: The NOAA El Niño Rapid Response Field Campaign. *Bull. Amer. Meteor. Soc.*, **99**, 975–1001, https://doi.org/10.1175/BAMS-D-16-0219.1.

ECMWF, 2009: ERA-Interim Project. Research Data Archive at the National Center for Atmospheric Research, Computational and Information Systems Laboratory, accessed 12 March 2018, https://doi.org/10.5065/D6CR5RD9.

Firl, G., 2017: Using the global modeling testbed single column model to test a newly developed convective parameterization. *28th Conf. on Weather Analysis and Forecasting/24th Conf. on Numerical Weather Prediction*, Seattle, WA, Amer. Meteor. Soc., 595, https://ams.confex.com/ams/97Annual/webprogram/Paper314680.html.

Frierson, D. M., 2007: Convectively coupled Kelvin Waves in an Idealized moist general circulation model. *J. Atmos. Sci.*, **64**, 2076–2090, https://doi.org/10.1175/JAS3945.1.

Goswami, B. B., B. Khouider, R. Phani, P. Mukhopadhyay, and A. J. Majda, 2017: Implementation and calibration of a stochastic multicloud convective parameterization in the NCEP Climate Forecast System (CFSv2). *J. Adv. Model. Earth Syst.*, **9**, 1721–1739, https://doi.org/10.1002/2017MS001014.

Gregory, D., J.-J. Morcrette, C. Jakob, A. M. Beljaars, and T. Stockdale, 2000: Revision of convection, radiation and cloud schemes in the ECMWF model. *Quart. J. Roy. Meteor. Soc.*, **126**, 1685–1710, https://doi.org/10.1002/qj.49712656607.

Hamill, T. M., and G. N. Kiladis, 2014: Skill of the MJO and Northern Hemisphere blocking in GEFS medium-range reforecasts. *Mon. Wea. Rev.*, **142**, 868–885, https://doi.org/10.1175/MWR-D-13-00199.1.

Han, J., and H. Pan, 2011: Revision of convection and vertical diffusion schemes in the NCEP Global Forecast System. *Wea. Forecasting*, **26**, 520–533, https://doi.org/10.1175/WAF-D-10-05038.1.

——, W. Wang, Y. C. Kwon, S. Hong, V. Tallapragada, and F. Yang, 2017: Updates in the NCEP GFS cumulus convection schemes with scale and aerosol awareness. *Wea. Forecasting*, **32**, 2005–2017, https://doi.org/10.1175/WAF-D-17-0046.1.

Harris, L. M., S. Lin, and C. Tu, 2016: High-resolution climate simulations using GFDL HiRAM with a stretched global grid. *J. Climate*, **29**, 4293–4314, https://doi.org/10.1175/JCLI-D-15-0389.1.

Hendon, H. H., and M. C. Wheeler, 2008: Some space–time spectral analyses of tropical convection and planetary-scale waves. *J. Atmos. Sci.*, **65**, 2936–2948, https://doi.org/10.1175/2008JAS2675.1.

Herzegh, P. H., and P. V. Hobbs, 1980: The mesoscale and microscale structure and organization of clouds and precipitation in mid-latitude cyclones. Part II: Warm frontal clouds. *J. Atmos. Sci.*, **37**, 597–611, https://doi.org/10.1175/1520-0469(1980)037<0597:TMAMSA>2.0.CO;2.

Hirons, L. C., P. Inness, F. Vitart, and P. Bechtold, 2013a: Understanding advances in the simulation of intraseasonal variability in the ECMWF model. Part I: The representation of the MJO. *Quart. J. Roy. Meteor. Soc.*, **139**, 1417–1426, https://doi.org/10.1002/qj.2060.

——, ——, ——, and ——, 2013b: Understanding advances in the simulation of intraseasonal variability in the ECMWF model. Part II: The application of process-based diagnostics. *Quart. J. Roy. Meteor. Soc.*, **139**, 1427–1444, https://doi.org/10.1002/qj.2059.

Hong, S.-Y., and H.-L. Pan, 1996: Nonlocal boundary layer vertical diffusion in a medium-range forecast model. *Mon. Wea. Rev.*, **124**, 2322–2339, https://doi.org/10.1175/1520-0493(1996)124<2322:NBLVDI>2.0.CO;2.

Houze, R. A., J. D. Locatelli, and P. V. Hobbs, 1976: Dynamics and cloud microphysics of the rainbands in an occluded frontal system. *J. Atmos. Sci.*, **33**, 1921–1936, https://doi.org/10.1175/1520-0469(1976)033<1921:DACMOT>2.0.CO;2.

Hovmöller, E., 1949: The trough-and-ridge diagram. *Tellus*, **1**, 62–66, https://doi.org/10.1111/j.2153-3490.1949.tb01260.x.

Huffman, G. J., and Coauthors, 2007: The TRMM Multisatellite Precipitation Analysis (TMPA): Quasi-global, multiyear, combined-sensor precipitation estimates at fine scales. *J. Hydrometeor.*, **8**, 38–55, https://doi.org/10.1175/JHM560.1.

——, E. Stocker, D. Bolvin, E. Nelkin, and R. Adler, 2012: TRMM version 7 3B42 and 3B43 data sets. NASA/GSFC, accessed 4 April 2019.

Janiga, M. A., C. J. Schreck, J. A. Ridout, M. Flatau, N. P. Barton, E. J. Metzger, and C. A. Reynolds, 2018: Subseasonal forecasts of convectively coupled equatorial waves and the MJO: Activity and predictive skill. *Mon. Wea. Rev.*, **146**, 2337–2360, https://doi.org/10.1175/MWR-D-17-0261.1.

Jones, C., J. Gottschalck, L. M. V. Carvalho, and W. Higgins, 2011: Influence of the Madden–Julian oscillation on forecasts of extreme precipitation in the contiguous United States. *Mon. Wea. Rev.*, **139**, 332–350, https://doi.org/10.1175/2010MWR3512.1.

Joyce, B., and J. Janowiak, 2005: NOAA CPC Morphing Technique (''CMORPH''). NOAA Climate Prediction Center, accessed 7 January 2014, http://www.cpc.ncep.noaa.gov/products/janowiak/cmorph_description.html.

Joyce, R. J., J. E. Janowiak, P. A. Arkin, and P. Xie, 2004: CMORPH: A method that produces global precipitation estimates from passive microwave and infrared data at high spatial and temporal resolution. *J. Hydrometeor.*, **5**, 487–503, https://doi.org/10.1175/1525-7541(2004)005<0487:CAMTPG>2.0.CO;2.

Kiladis, G. N., M. C. Wheeler, P. T. Haertel, K. H. Straub, and P. E. Roundy, 2009: Convectively coupled equatorial waves. *Rev. Geophys.*, **47**, RG2003, https://doi.org/10.1029/2008RG000266.

Kim, D., A. H. Sobel, D. M. W. Frierson, E. D. Maloney, and I.-S. Kang, 2011: A systematic relationship between intraseasonal variability and mean state bias in AGCM simulations. *J. Climate*, **24**, 5506–5520, https://doi.org/10.1175/2011JCLI4177.1.

Kleist, D. T., and K. Ide, 2015: An OSSE-based evaluation of hybrid variational–ensemble data assimilation for the NCEP GFS. Part II: 4DEnVar and hybrid variants. *Mon. Wea. Rev.*, **143**, 452–470, https://doi.org/10.1175/MWR-D-13-00350.1.

Lim, Y., S. Son, and D. Kim, 2018: MJO prediction skill of the subseasonal-to-seasonal prediction models. *J. Climate*, **31**, 4075–4094, https://doi.org/10.1175/JCLI-D-17-0545.1.

Lin, S., 2004: A "vertically lagrangian" finite-volume dynamical core for global models. *Mon. Wea. Rev.*, **132**, 2293–2307, https://doi.org/10.1175/1520-0493(2004)132<2293:AVLFDC>2.0.CO;2.

——, and R. B. Rood, 1996: Multidimensional flux-form semi-Lagrangian transport schemes. *Mon. Wea. Rev.*, **124**, 2046–2070, https://doi.org/10.1175/1520-0493(1996)124<2046:MFFSLT>2.0.CO;2.

Lin, J., M. Lee, D. Kim, I. Kang, and D. M. Frierson, 2008: The impacts of convective parameterization and moisture triggering on AGCM-simulated convectively coupled equatorial waves. *J. Climate*, **21**, 883–909, https://doi.org/10.1175/2007JCLI1790.1.

Lin, Y.-L., R. D. Farley, and H. D. Orville, 1983: Bulk parameterization of the snow field in a cloud model. *J. Climate Appl. Meteor.*, **22**, 1065–1092, https://doi.org/10.1175/1520-0450(1983)022<1065:BPOTSF>2.0.CO;2.

Liu, C., and E. Zipser, 2014: Differences between the surface precipitation estimates from the TRMM Precipitation Radar and Passive Microwave Radiometer version 7 products. *J. Hydrometeor.*, **15**, 2157–2175, https://doi.org/10.1175/JHM-D-14-0051.1.

Magnusson, L., J. Chen, S. Lin, L. Zhou, and X. Chen, 2019: Dependence on initial conditions vs. model formulations for medium-range forecast error variations. *Quart. J. Roy. Meteor. Soc.*, **145**, 2085–2100, https://doi.org/10.1002/qj.3545.

Mapes, B. E., S. Tulich, J. L. Lin, and P. Zuidema, 2006: The mesoscale convection life cycle: Building block or prototype for large scale tropical waves? *Dyn. Atmos. Oceans*, **42**, 3–29, https://doi.org/10.1016/j.dynatmoce.2006.03.003.

Matsuno, T., 1966: Quasi-geostrophic motions in the equatorial area. *J. Meteor. Soc. Japan*, **44**, 25–43, https://doi.org/10.2151/jmsj1965.44.1_25.

NOAA, 2015: CMORPHv1.0: NOAA CPC Morphing Technique ("CMORPH"), version 1.0, CRT. NOAA Center for Weather and Climate Prediction, accessed August 2017, http://ftp.cpc.ncep.noaa.gov/precip/CMORPH_V1.0/CRT/.

Orbe, C., L. D. Oman, S. E. Strahan, D. W. Waugh, S. Pawson, L. L. Takacs, and A. M. Molod, 2017: Large-scale atmospheric transport in GEOS replay simulations. *J. Adv. Model. Earth Syst.*, **9**, 2545–2560, https://doi.org/10.1002/2017MS001053.

Pan, H.-L., and W.-S. Wu, 1995: Implementing a mass flux convective parameterization package for the NMC Medium-Range Forecast model. NMC Office Note 409, 40 pp., https://repository.library.noaa.gov/view/noaa/11429.

Park, S., 2014: A Unified Convection Scheme (UNICON). Part I: Formulation. *J. Atmos. Sci.*, **71**, 3902–3930, https://doi.org/10.1175/JAS-D-13-0233.1.

Petch, J., A. Hill, L. Davies, A. Fridlind, C. Jakob, Y. Lin, S. Xie, and P. Zhu, 2014: Evaluation of intercomparisons of four different types of model simulating TWP-ICE. *Quart. J. Roy. Meteor. Soc.*, **140**, 826–837, https://doi.org/10.1002/qj.2192.

Putman, W., and S. Lin, 2007: Finite-volume transport on various cubed-sphere grids. *J. Comput. Phys.*, **227**, 55–78, https://doi.org/10.1016/j.jcp.2007.07.022.

Rabier, F., H. Jarvinen, E. Klinker, J.-F. Mahfouf, and A. Simmons, 2000: The ECMWF operational implementation of four-dimensional variational assimilation. I: Experimental results with simplified physics. *Quart. J. Roy. Meteor. Soc.*, **126A**, 1143–1170, https://doi.org/10.1002/qj.49712656415.

Sardeshmukh, P. D., and B. J. Hoskins, 1988: The generation of global rotational flow by steady idealized tropical divergence. *J. Atmos. Sci.*, **45**, 1228–1251, https://doi.org/10.1175/1520-0469(1988)045<1228:TGOGRF>2.0.CO;2.

Schreck, C. J., J. M. Cordeira, and D. Margolin, 2013: Which MJO events affect North American temperatures? *Mon. Wea. Rev.*, **141**, 3840–3850, https://doi.org/10.1175/MWR-D-13-00118.1.

Siebesma, A. P., P. M. M. Soares, and J. Teixeira, 2007: A combined eddy-diffusivity mass-flux approach for the convective boundary layer. *J. Atmos. Sci.*, **64**, 1230–1248, https://doi.org/10.1175/JAS3888.1.

Sobel, A., and E. Maloney, 2013: Moisture modes and the eastward propagation of the MJO. *J. Atmos. Sci.*, **70**, 187–192, https://doi.org/10.1175/JAS-D-12-0189.1.

Takacs, L. L., M. J. Suárez, and R. Todling, 2018: The stability of incremental analysis update. *Mon. Wea. Rev.*, **146**, 3259–3275, https://doi.org/10.1175/MWR-D-18-0117.1.

Thayer-Calder, K., and D. A. Randall, 2009: The role of convective moistening in the Madden–Julian oscillation. *J. Atmos. Sci.*, **66**, 3297–3312, https://doi.org/10.1175/2009JAS3081.1.

Tiedtke, M., W. A. Heckley, and J. Slingo, 1988: Tropical forecasting at ECMWF: The influence of physical parameterization on the mean structure of forecasts and analyses. *Quart. J. Roy. Meteor. Soc.*, **114**, 639–644, https://doi.org/10.1002/qj.49711448106.

Troen, I., and L. Mahrt, 1986: A simple model of the atmospheric boundary layer sensitivity to surface evaporation. *Bound.-Layer Meteor.*, **37**, 129–148, https://doi.org/10.1007/BF00122760.

Vitart, F., 2014: Evolution of ECMWF sub-seasonal forecast skill scores. *Quart. J. Roy. Meteor. Soc.*, **140**, 1889–1899, https://doi.org/10.1002/qj.2256.

Wheeler, M., and G. N. Kiladis, 1999: Convectively coupled equatorial waves: Analysis of clouds and temperature in the wavenumber–frequency domain. *J. Atmos. Sci.*, **56**, 374–399, https://doi.org/10.1175/1520-0469(1999)056<0374:CCEWAO>2.0.CO;2.

Xu, K.-M., and D. A. Randall, 1999: A sensitivity study of radiative–convective equilibrium in the Tropics with a convection-resolving model. *J. Atmos. Sci.*, **56**, 3385–3399, https://doi.org/10.1175/1520-0469(1999)056<3385:ASSORC>2.0.CO;2; Corrigendum, **57**, 1958, https://doi.org/10.1175/1520-0469(2000)057<1958:C>2.0.CO;2.

Yanai, M., S. Esbensen, and J.-H. Chu, 1973: Determination of bulk properties of tropical cloud clusters from large-scale heat and moisture budgets. *J. Atmos. Sci.*, **30**, 611–627, https://doi.org/10.1175/1520-0469(1973)030<0611:DOBPOT>2.0.CO;2.

Zhang, C., 2005: Madden-Julian Oscillation. *Rev. Geophys.*, **43**, RG2003, https://doi.org/10.1029/2004RG000158.